

Key Points:

- Zircon (U-Th-Sm)/He data suggests that pre-Andean exhumation of Salta rift basement highs occurred in the Early Cretaceous (140-115 Ma)
- Apatite (U-Th-Sm)/He and fission track data indicate a late Oligocene-early Miocene (26-16 Ma) onset of exhumation in the Tilcara Range
- Andean exhumation overall propagated in-sequence eastward, but thermal models indicate the possibility of local out-of-sequence movement

Supporting Information:

Supporting Information may be found in the online version of this article.

Correspondence to:

W. S. M. T. van Kooten,
vankooten@uni-potsdam.de

Citation:

van Kooten, W. S. M. T., Sobel, E. R., del Papa, C. E., Payrola, P., & Glodny, J. (2022). Constraining Andean propagation of exhumation at the limit of the Eastern Cordillera, NW Argentina, using low-temperature thermochronology in a structural context. *Tectonics*, *41*, e2022TC007342. <https://doi.org/10.1029/2022TC007342>

Received 6 APR 2022

Accepted 20 JUL 2022

© 2022. The Authors.

This is an open access article under the terms of the [Creative Commons Attribution-NonCommercial-NoDerivs License](#), which permits use and distribution in any medium, provided the original work is properly cited, the use is non-commercial and no modifications or adaptations are made.



Constraining Andean Propagation of Exhumation at the Limit of the Eastern Cordillera, NW Argentina, Using Low-Temperature Thermochronology in a Structural Context

Willemijn S. M. T. van Kooten¹ , Edward R. Sobel¹ , Cecilia E. del Papa², Patricio Payrola³ , and Johannes Glodny⁴ 

¹University of Potsdam, Potsdam, Germany, ²Cicterra, CONICET-University of Córdoba, Córdoba, Argentina, ³National University of Salta, Salta, Argentina, ⁴GFZ German Research Center for Geosciences, Potsdam, Germany

Abstract Within the Central Andes of NW Argentina, the spatiotemporal distribution and style of deformation is strongly influenced by pre-Cenozoic heterogeneities, mostly related to the Salta rift extension in the Cretaceous. At the enigmatic junction of the thin-skinned Subandean belt and the thick-skinned Santa Barbara System, the Tilcara Range and adjacent San Lucas block, located within the Eastern Cordillera, show thermochronological and field evidence of multiple exhumation events. Mesozoic (140-115 Ma), pre-Andean exhumation of basement highs is constrained by unconformities between basement and syn-rift strata, as well as zircon (U-Th-Sm)/He cooling ages. Cenozoic Andean exhumation is quantified by apatite (U-Th-Sm)/He and fission track cooling ages, which were reset between the Late Cretaceous and Miocene. These data show that the westernmost Tilcara Range began exhuming in the late Oligocene-early Miocene (26-16 Ma), after which exhumation propagated to the border of the Eastern Cordillera in the middle Miocene (22-10 Ma). The onset of rapid exhumation in the San Lucas block, which is located east of the Tilcara Range, occurred in the late Miocene (10-8 Ma) in its western part, and in the late Miocene-early Pliocene (6-4 Ma) in its eastern part. Internal deformation of the San Lucas block, disturbing zircon (U-Th-Sm)/He and apatite fission track age patterns, predates propagation of rapid exhumation. The here presented low-temperature thermochronology data set thus quantifies the multi-phase exhumation history of the Eastern Cordillera of NW Argentina and constrains the timing of Andean propagation of exhumation within the Eastern Cordillera and the adjacent structural transition zone.

1. Introduction

The Andean orogenic belt is commonly divided into morphotectonic provinces (e.g., Carrapa et al., 2011; Jordan et al., 1983; Kley, 1996; Strecker et al., 2007) that are characterized by their unique structural styles (Figure 1a). Especially the eastern limit of the Central Andes in southern Bolivia and NW Argentina shows rapid structural changes along-strike between the Inter-/Subandean Zone and the Santa Barbara System, which form the foreland of the Eastern Cordillera. Previous studies of the transition from the Eastern Cordillera to the Inter- and Subandean Zone, their structural characteristics and their exhumation history have focused heavily on the Bolivian part of the fold-and-thrust belt (Anderson et al., 2017, 2018; Arriagada et al., 2008; Barnes et al., 2008; DeCelles & Horton, 2003; Echavarría et al., 2003; Eichelberger et al., 2013; Gubbels et al., 1993; Horton, 2005; Kley, 1996; McQuarrie, 2002; Müller et al., 2002; Rak et al., 2017; Roeder, 1988), where hydrocarbon exploration has provided a large data set for detailed structural modeling. In contrast, the limit of the Eastern Cordillera in Argentina and the transition from the Subandean Zone to the Santa Barbara System are poorly constrained; in particular, the cause for the abrupt termination of the Interandean and Subandean fold-and-thrust belt south of 23°S remains an enigma to be solved.

The complex geological history of the Central Andes, comprising multiple wide-reaching phases of contraction and extension (e.g., Carrera et al., 2006; Heredia et al., 2018; Ramos, 2008), is responsible for creating heterogeneities that were reactivated during Andean shortening and thus greatly influences the present structure of the Andean orogeny and the distribution of its morphotectonic provinces. Of all preceding phases, the widespread Salta rift basin has played a major role in controlling the localization and characteristics of Andean deformation within the Eastern Cordillera. There are many excellent examples of reactivation and inversion of Cretaceous extensional faults within the Eastern Cordillera and Santa Barbara System (e.g., Carrera et al., 2006; Kley & Monaldi, 2002; Kley et al., 2005; Kortyna et al., 2019; Seggiaro et al., 2017), which have mostly been studied

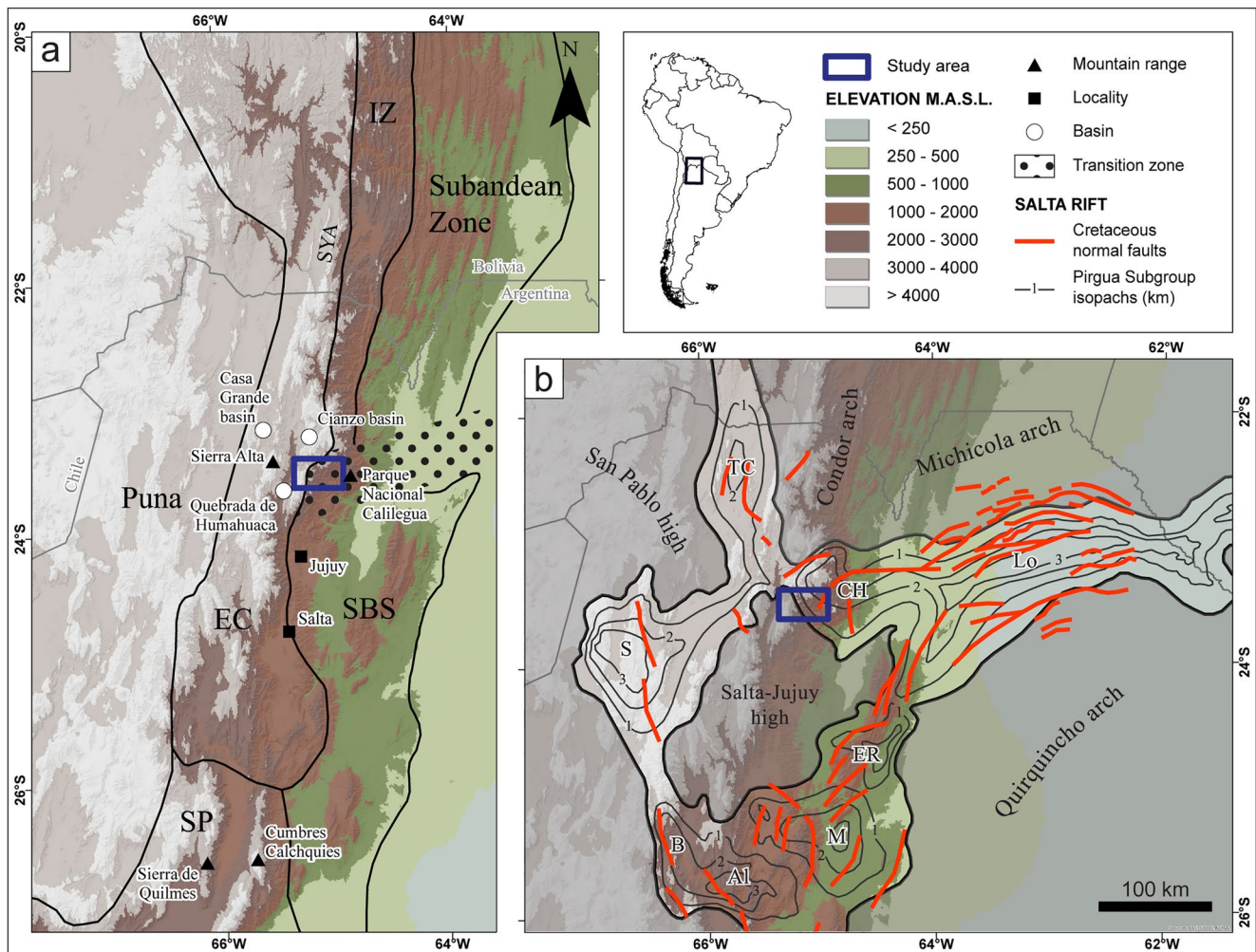


Figure 1. (a) Overview of the Central Andes between 20°S and 27°S with its morphotectonic provinces, modified from Jordan et al. (1983). EC: Eastern Cordillera, IZ: Interandean Zone, SBS: Santa Barbara System, SP: Sierras Pampeanas. The transition zone between the Inter- and Subandean Zone, SBS and EC is marked. Sama-Yunchará anticlinorium (SYA) is indicated. (b) Overview of the Salta rift basin including sub-basins (TC: Tres Cruces, CH: Cerro Hermoso, Lo: Lomas de Olmedo, S: Sey, ER: El Rey, M: Metán, Al: Alemania, B: Brealito), showing syn-rift isopachs from Salfity and Marquillas (1994) and the location of structural highs (gray). Locations of Cretaceous normal faults (red) from Starck (2011). Blue square represents the area shown in Figure 2.

qualitatively using stratigraphic and structural relations based on field data. Complementing qualitative studies, low-temperature thermochronology, when placed in a structural context, is a powerful instrument to quantify both timing and magnitude of fault-related exhumation within fold-and-thrust belts and provides the opportunity to date multiple exhumation events related to the reactivation of pre-existing structures.

In this study we present a new robust data set of low-temperature thermochronologic cooling ages constraining consecutive phases of exhumation within the Eastern Cordillera of NW Argentina. We performed apatite (U-Th-Sm)/He (AHe), apatite fission track (AFT) and zircon (U-Th-Sm)/He (ZHe) dating on 26 samples that are arranged in W-E vertical and horizontal transects crossing the Tilcara Range orographic barrier and adjacent Yungas lowlands. Using an improved structural framework and multi-sample thermal modeling, we reconstruct the reactivation of pre-Cenozoic heterogeneities in the course of the Andean orogeny. The resulting model focuses on the boundary of the Eastern Cordillera and the transition zone between the Subandean Zone and Santa Barbara System at 23.5°S, and sheds new light on propagation of deformation in time and space at the limit of this major Andean fold-and-thrust belt.

2. Geological Setting

The Eastern Cordillera of NW Argentina is bordered by the Inter- and Subandean Zone to the east and the Altiplano-Puna plateau to the west (Figure 1a). Whereas the Interandean Zone is increasingly integrated into the Eastern Cordillera, the Subandean Zone abruptly terminates at 23°S and is replaced by the Santa Barbara System south of 23.5°S (Kley & Monaldi, 2002). The Eastern Cordillera and Santa Barbara System transition into the Sierras Pampeanas toward the south (Figure 1a). Concurrently, the structural style changes rapidly from a classic thin-skinned fold-and-thrust belt in the Bolivian Subandean Zone (Dunn et al., 1995; Eichelberger et al., 2013; McQuarrie, 2002) to the thick-skinned broken foreland basins of the Santa Barbara System and the Sierras Pampeanas, where basement blocks are uplifted along reactivated, pre-existing faults (e.g., Kley & Monaldi, 2002; Kley et al., 1999; Zapata et al., 2019). Although Jordan et al. (1983) proposed a correlation between tectonic disparities and the transition from steep (~30°) to flat (~5°–10°) subduction, more recent studies (Anderson et al., 2007; Gans et al., 2011; Horton, 2018; Linkimer et al., 2020; Ramos et al., 2002) show that this transition zone is narrower and located further south, and that there is a poor correlation between changes in structural style and slab angle. Kley and Monaldi (2002) argue that the sharp boundaries of the Santa Barbara System form a pronounced contrast to the smooth variation of slab inclination and suggest that stratigraphic disparities might instead have a major impact on the current structural segmentation of the Andes. Similarly, McGroder et al. (2015) propose a strong influence of inherited crustal elements within the South American plate on structural styles and hydrocarbon resources within the Central Andes. Indeed, many authors (e.g., Carrera et al., 2006; Grier et al., 1991; Kley & Monaldi, 2002; Kley et al., 2005; Kortyna et al., 2019; McGroder et al., 2015) have demonstrated that inherited anisotropies from Paleozoic and Cretaceous tectonism strongly influenced the present-day deformational pattern in the Eastern Cordillera between 23°S and 24°S.

At the far eastern limit of the Eastern Cordillera, the Tilcara Range strikes N-S, showing high topography with peak elevations just below 5,000 m. The Tilcara Range is bounded to the east by a high-angle, north-striking, east-vergent reverse fault that is hereafter referred to as the Tilcara Range Frontal Fault (Figure 2). The San Lucas block is located directly east of this reverse fault. The basement of the Tilcara Range consists of the late Ediacaran-early Cambrian Puncoviscana Formation, deposited in the Puncoviscana foreland basin bordering the Pampean orogen (Aceñolaza, 2003; Einhorn et al., 2015; Escayola et al., 2011; Pearson et al., 2012). It encompasses weakly metamorphosed (Escayola et al., 2011; Pearson et al., 2012) alternating claystones, siltstones and sandstones with an estimated total thickness of >2,000 m (Aceñolaza, 2003). The Pampean-Tilcaric unconformity (Escayola et al., 2011; Turner & Mendez, 1975) separates the Puncoviscana Formation from the overlying middle to late Cambrian Mesón Group and marks the end of the Pampean cycle (Adams et al., 2011).

The Mesón Group consists of up to 3,000 m thick marine siliciclastic rocks (Aceñolaza, 2003; Moya, 1998; Sánchez & Salfity, 1999), although thickness varies locally, and is divided into upper and lower coarse-grained, cliff-forming quartzite units, and the middle, finer-grained Campanario Formation. An unconformity exists between the Mesón Group and the overlying upper Cambrian-lower Ordovician Santa Victoria Group (Rahl et al., 2018; Vaucher et al., 2020). The Santa Victoria Group consists of alternating quartz-rich sandstones and shales with a thickness of a few thousands meters (Aceñolaza, 2003; Moya, 2015). Within the Tilcara Range, large parts were eroded and the preserved Ordovician strata can locally be as thin as 500 m (Buatois et al., 2006).

The Precambrian to Ordovician sedimentary basement strata were deformed during the Oclöyic phase (middle Ordovician-middle Silurian or Devonian) (Bahlburg et al., 2000; Heredia et al., 2018; Otamendi et al., 2020; Ramos, 2008; Seggiaro et al., 2017). The Oclöyic phase induced uplift in the area of the present-day Puna and Eastern Cordillera (Starck et al., 1992) and led to an eastward migration of foreland basins. Alonso et al. (2012, p. 1846) consider the Eastern Cordillera the “non-metamorphic part of the Oclöyic foreland thrust belt”. Structures in the Eastern Cordillera that were formed during the Oclöyic orogeny show a dominant north-strike and east vergence (Hongn et al., 2010) and are thus positioned favorably for Andean reactivation (Heredia et al., 2018; Seggiaro et al., 2017). Salfity and Marquillas (1994) propose that compressional deformation related to the Oclöyic orogeny also affected the Tilcara Range. However, Ordovician normal faulting has also been recorded in the Eastern Cordillera (Seggiaro et al., 2008, 2017; Villagrán et al., 2015) and not in all cases the original geometry and slip of Paleozoic structures is clearly defined. Although Silurian to Carboniferous strata were deposited (González & Tchilinguirian, 2003; Starck, 1995), they were largely eroded prior to Cretaceous sedimentation (Salfity & Marquillas, 1994; Starck, 1995) and the majority of Cretaceous-Paleogene strata were deposited unconformably on top of Ordovician rocks (Figure 2b).

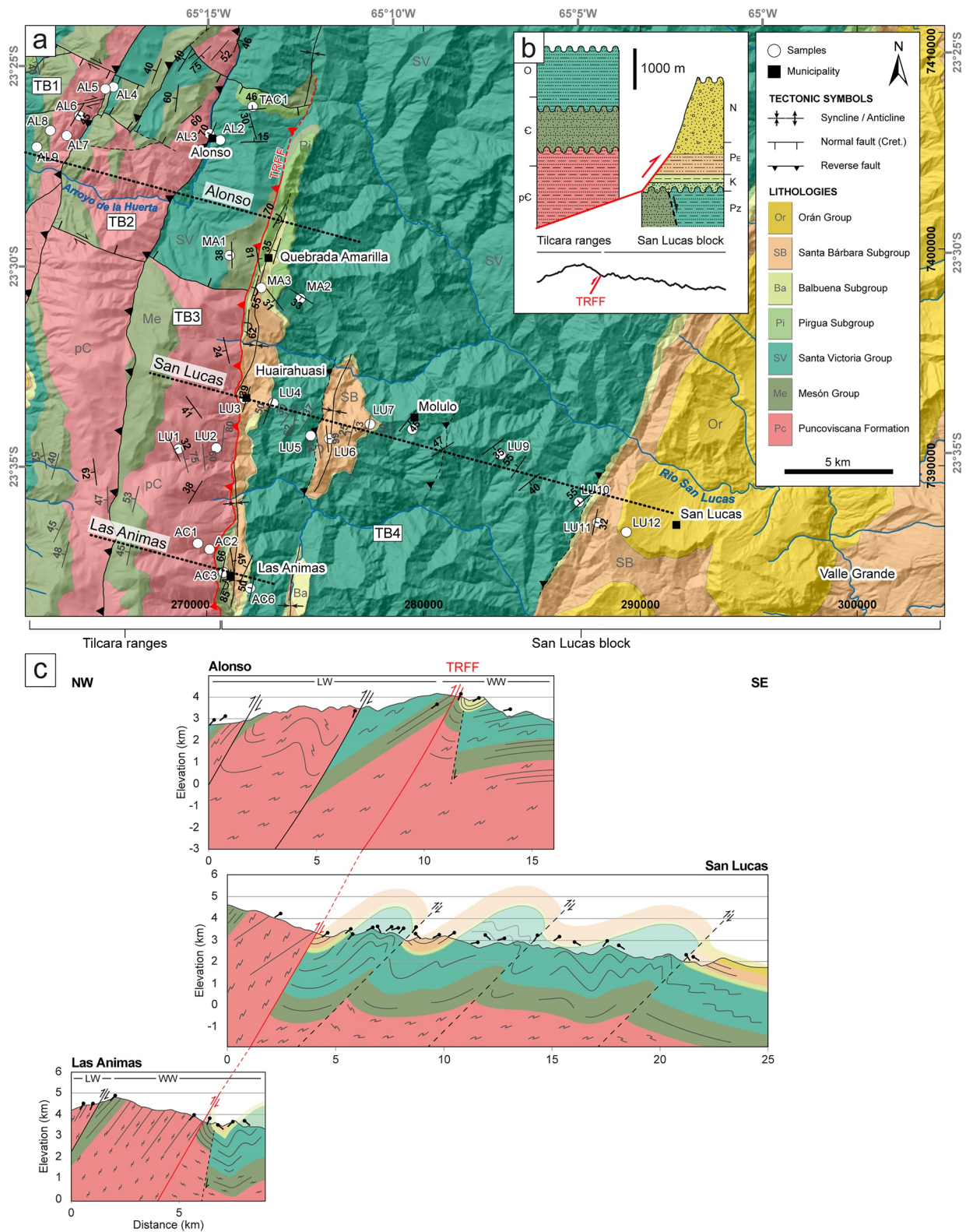


Figure 2.

From the Late Jurassic to Early Cretaceous, the opening of the South Atlantic Ocean caused extension in the location of the Cenozoic Central Andes and the development of the Salta rift basin, which covered most of NW Argentina (Marquillas et al., 2005; Salfity & Marquillas, 1994). The Salta basin hosts a thick succession of syn- and post-rift sediments of the Salta Group (Turner, 1959) that were deposited from the lower Cretaceous up to the middle Eocene (Marquillas et al., 2005; Salfity & Marquillas, 1994). The Salta Group is divided into the syn-rift Pirgua Subgroup (Reyes & Salfity, 1973) and the post-rift Balbuena and Santa Bárbara Subgroups (Moreno, 1970). Further subdivisions and their spatial distribution vary regionally, depending on the specific depocenter.

One of the Salta rift depocenters is the NW-SE striking Lomas de Olmedo sub-basin. It is delimited to the north by the Michicola arch and to the south by the Quirquincho arch. The Condor arch and the Salta-Jujuy high confine the basin to the west (Figure 1b). The area of the Tilcara Range was part of the westernmost Lomas de Olmedo sub-basin during the late syn-rift and post-rift stages. However, Salfity and Marquillas (1994) suggest that the very first sedimentary infill, consisting of the lowermost Pirgua Subgroup, was shed into a separate depocenter known as Cerro Hermoso (Figure 1b). Within the Tilcara Range, the Pirgua Subgroup is relatively thin, especially compared with its thickness of >2,500 m within the Cianzo syncline farther north (Boll et al., 1989). The post-rift strata were mainly accommodated by thermal subsidence (Marquillas et al., 2005; Viramonte et al., 1999) and possibly early flexural loading from the Altiplano-Puna plateau (Becker et al., 2015). Seismic sections show that normal fault activity related to rifting in the Lomas de Olmedo sub-basin commenced no later than the Cretaceous and continued up to the Paleocene (Starck, 2011). Some authors argue that local conglomerate levels, NE-directed paleoflow and the extraordinarily large spatial distribution of the Santa Bárbara Subgroup indicate an early influence of the Andean orogenic wedge in the late Paleocene-Eocene (e.g., DeCelles et al., 2011). Ultimately, the late Eocene-early Oligocene onset of Andean shortening in the Puna and Eastern Cordillera ended the deposition of the Salta Group (Carrapa et al., 2011; Coutand et al., 2001; Marquillas et al., 2005; Salfity & Marquillas, 1994).

Following the uplift in the Puna and Eastern Cordillera during the late Eocene or early Oligocene (Carrapa & DeCelles, 2008; Carrapa et al., 2011; Coutand et al., 2001; DeCelles et al., 2007, 2011; Henríquez et al., 2020, 2022), the Salta Group was buried by foreland deposits of the Orán Group (Boll & Hernández, 1986; Salfity & Marquillas, 1994). Whereas most studies agree that its lower part (Metán Subgroup) was deposited in a widespread basin (Coutand et al., 2001; DeCelles et al., 2011; Siks & Horton, 2011), the younger tectonosedimentary history has been debated. Some authors conclude that from the late Oligocene-late Miocene on, clastic sediments were deposited in smaller, fully or partly isolated depocenters generated during the uplift of the Eastern Cordillera (Becker et al., 2015; Siks & Horton, 2011; Strecker et al., 2007). Thus, the Orán Group directly documents the propagation of Andean deformation from the Puna to the Eastern Cordillera (Becker et al., 2015). Other studies (Carrapa et al., 2012; DeCelles et al., 2011) argue that upper Miocene-Quaternary sediments represent wedge-top accumulations that were deposited in a connected regional foreland basin system.

2.1. Timing of Uplift

Tectonic shortening related to Andean mountain building in the Puna and Eastern Cordillera (between 23.5°S and 24°S) began in the early Paleogene with the inversion of extensional Salta Rift structures. Relief formation commenced in the middle-late Eocene (Montero-López et al., 2020). Although the proto-Sierra Alta (Figure 1), west of the Tilcara Range, started uplifting in the Paleogene (Montero-López et al., 2020), Pingel et al. (2013) (with data from Deeken et al., 2006; Reynolds et al., 2000, 2001; Siks & Horton, 2011) show that uplift was most pronounced at ~15 Ma. Undeformed deposits that unconformably overlie folded Ordovician to Miocene strata above the San Juan de Oro geomorphic surface, south of the Bolivian border, indicate that major deformation in the western Eastern Cordillera terminated at 9 Ma (Allmendinger & Zapata, 2000). In contrast, Streit et al. (2017)

Figure 2. (a) Geological map of the Tilcara Range and San Lucas block revised from González and Tchilinguirian (2003) and Jiron (2015). Coordinates are shown as UTM WGS84 zone 20K (inside frame) and degree-minutes-seconds (outside frame). TB1–TB4 mark tectonic blocks. Dotted lines depict Alonso, San Lucas and Las Animas transects. The Tilcara Range Frontal Fault (TRFF) is marked in red. Measurements marked in gray are from Jiron (2015). (b) Schematic overview of structural and stratigraphic relationships between the basement and Cretaceous-Paleogene strata within the Tilcara Range and San Lucas block (TB4). Topographic section shows the difference in altitude between the Tilcara Range and San Lucas block. (c) Schematic cross-sections of the Alonso, San Lucas and Las Animas transects. The Tilcara Range Frontal Fault is marked in red. The leeward (LW) and windward (WW) sides of the Tilcara Range are indicated. Folding in Precambrian-Paleozoic strata is shown schematically.

show that fluvial incision at the Casa Grande basin (Figure 1) outlet was only outpaced by the rate of uplift of the Sierra Alta, bounding this basin to the east, between 3.8 and 0.8 Ma, which they attribute to increased sediment supply connected to enhanced precipitation and increased uplift rates. This implies that range uplift west of the Humahuaca valley continued during Pliocene-Pleistocene times. Deformation in general propagated eastward (Anderson et al., 2017, 2018; DeCelles et al., 2007, 2011; Deeken et al., 2006; Henríquez et al., 2019, 2020), with proposed periods of out-of-sequence deformation (e.g., Henríquez et al., 2022), and reached the Tilcara Range at ~10–4 Ma (Henríquez et al., 2022; Pingel et al., 2013, 2014; Siks & Horton, 2011). Early uplift of the Tilcara Range and its northern continuation is well documented in the Cianzo basin, ~20 km east of Humahuaca, where the Orán Group records a changing geological setting from a widespread foreland basin to a restricted intermontane basin in the late Miocene (Siks & Horton, 2011). Uplift of the Tilcara Range formed an orographic barrier, disrupting drainage patterns within the Humahuaca basin west of the Tilcara Range after 4.2 Ma, based on changes in paleoflow directions and increasingly proximal facies (Pingel et al., 2013). Consequently, surface uplift of the Tilcara Range before 4.2 Ma was not sufficient to disrupt fluvial connectivity (Streit et al., 2017). These results clearly suggest Pliocene or younger uplift of the Tilcara Range. Pingel et al. (2019) show that an abrupt decrease of denudation rates is in agreement with the establishment of an orographic barrier after 3 Ma: whereas pre-3 Ma rates were similar to modern-day denudation rates (0.49 and 0.58 mm/a) on the wet side of the Tilcara Range (Bookhagen & Strecker, 2012; Schildgen et al., 2016), post-3 Ma rates show a tenfold decrease (Pingel et al., 2019), indicating dryer conditions on the leeward side of the orographic barrier and a strong erosional gradient, which might affect low-temperature thermochronology cooling ages.

3. Methods

3.1. Mapping and Cross-Section Construction

The revised geological map (Figure 2a) was constructed based on field data from our 2019 and 2021 campaigns, existing measurements by Jiron (2015) and descriptions and interpretations from González and Tchilinguirian (2003). We used satellite imagery (Google, n.d.; Esri, 2021) to interpolate geological boundaries in areas where no field-based data was available. The revised map was digitized using the Esri ArcGIS® software ArcMap™ v10.5.1 on a scale of 1:5,000. Three parallel, WNW-ESE striking, unbalanced cross-sections were constructed in the software MOVE v2019.1 (Petroleum Experts, 2020), hereafter referred to as the Alonso, San Lucas and Las Animas transects (Figure 2c). We used the kink band method (Suppe, 1983) to create horizons whenever viable. Parallel formation boundaries were created, assuming constant thickness and a negligible angular relationship between the Santa Bárbara and the Balbuena subgroups. We used thickness measurements for Cretaceous-Paleogene strata from nearby stratigraphic sections (Boll et al., 1989) to estimate the viability of the sections. Because movement planes of major faults do not crop out, we qualitatively inferred the most probable fault orientation from the approximate intersection of major faults from satellite imagery with the digital elevation model (DEM) (Copernicus WorldDEM-30, 2021).

3.2. Sample Selection and Preparation

We collected 26 samples along three W-E transects crossing the Tilcara Range from the Quebrada de Humahuaca to Valle Grande (Figure 2c). The aim was to sample vertical transects for thermochronologic analysis and to access different structural positions within the tectonic blocks. Preliminary mineral separates (i.e., crushing, sieving, magnetic separation with strong hand magnet) were conducted at the National University of Salta. Further processing at the University of Potsdam included (a) magnetic separation, using a Frantz® magnetic separator with a frontal angle of 10°, a side angle of 10° and a current of 1.2 A, (b) treatment of the non-magnetic fraction with 10% acetic acid to remove carbonate and 3% H₂O₂ to remove clay and organic matter, and (c) density separation using Sodium Polytungstate (SPT; $\rho = 2.86 \text{ g/cm}^3$) and Diiodomethane (DI; $\rho = 3.3 \text{ g/cm}^3$).

3.3. Single-Grain (U-Th-Sm)/He Thermochronology

Low-temperature (U-Th-Sm)/He apatite and zircon (AHe and ZHe, respectively) thermochronology is based on α -particle ejection associated with the decay of U, Th and Sm parent isotopes. He atoms (α particles) are retained within apatite on geological timescales at temperatures below 40°C and are emitted at temperatures above 85°C (Wolf et al., 1998). This temperature interval “where helium is neither quantitatively retained nor lost

by diffusion” (Wolf et al., 1998, p. 105) is called the apatite partial retention zone (APRZ). The closure temperature (T_c) for the (U-Th-Sm)/He system varies with cooling rate, crystal size and radiation damage; a typical T_c is approximately 68°C for apatite (Farley, 2000). For zircons, the partial retention zone (ZPRZ) is between 170 and 190°C with an average experimental closure temperature of 183°C (Reiners et al., 2004). Ideal crystals for (U-Th-Sm)/He thermochronology should be euhedral with a diameter of >60 μm and free of inclusions, fractures and zoning.

We analyzed 26 samples from the basement and sedimentary strata of the Tilcara Range and San Lucas block using AHe and/or ZHe thermochronology. Aliquots were carefully hand-picked with a binocular polarizing microscope to eliminate grains with visible inclusions and/or fractures. Due to the detrital nature of the sandstone samples, the majority of the grains have a rounded geometry with frosted surfaces, potentially obscuring small inclusions and hairline fractures within the crystal. Although grains were carefully picked, we cannot fully exclude this cause of dispersion in detrital samples. Grain dimensions (width, length of prism, and total length) and the number of terminations were recorded for all grains. Aliquots were packed in Pt (for apatite) or Nb (for zircon) tubes and loaded into the Australian Scientific Instruments (ASI) Alphachron He extraction and analysis system at the University of Potsdam. Aliquots were heated twice with a 978 nm diode laser at 8 A for 5 min for apatite, or at 12 A for 10 min for zircon to achieve full He degassing. Two zircon aliquots were heated four times (see Table S1), because of residual He in the first re-extract. The resulting gas was purified using a SAES AP10N hot getter and analyzed using a Pfeiffer Prisma 200 Quadrupole mass spectrometer. The aliquots were then transferred to the German Research Center for Geosciences (GFZ) Potsdam for analysis of U, Th, and Sm abundances by isotope dilution. The grains were spiked with ^{235}U , ^{230}Th , and ^{149}Sm , dissolved, and then analyzed on a Thermo Element 2 XR ICP-MS. Additional analytical data are provided in Zhou et al. (2017) and Galetto et al. (2021). (U-Th-Sm)/He ages were calculated following the equations in Meesters and Dunai (2005) using the He, U, Th, and Sm abundances, an alpha-ejection correction factor (Ft) (Farley et al., 1996; Ketcham et al., 2011) obtained from the measured grain dimensions, and the alpha-particle stopping distance from Ketcham et al. (2011). We report (U-Th-Sm)/He ages with a weighted error (Table S1), which considers the relative contribution of each parent isotope to the total He production.

Weighted mean ages (Table 1) excluding outliers were calculated in IsoplotR using a random effects model that considers both the analytical uncertainty and an overdispersion term as sources of uncertainty (Vermeesch, 2018). AHe outliers are defined as aliquots that show $\text{Th}/^{238}\text{U} > 100$, or a combination of $\text{U} < 2$ ppm and 2σ (of corrected age) > 1.5 Ma. Furthermore, AHe aliquots are considered outliers if the single-grain age $\pm 2\sigma$ is greater than the sample's AFT age $\pm 1\sigma$ or if the single-grain ages show an exceptionally large amount of He compared to the amount of U, pointing toward the presence of an undissolved inclusion. ZHe outliers were defined by re-assessing grain geometry and characteristics and comparing these with single-grain ages. Excluded aliquots are marked in Table S1 and are ignored for both the weighted mean age calculation and further thermal history modeling. None of the AHe samples showed a positive age-eU trend corresponding to Flowers et al. (2009), although two samples showed a positive age-Ft and age-equivalent sphere radius (ESR) trend. Three ZHe samples showed positive age-eU trends, characteristic of zircons with $< 1,500$ ppm eU according to the radiation damage model of Guenther et al. (2013). One sample showed a negative age-eU trend with high overall eU, which can be attributed to increasing He diffusivity due to the interconnection of damage zones in the zircons (Guenther et al., 2013). Age-Ft and age-ESR relationships are seen in two ZHe samples. For samples with age-eU and/or age-Ft relationships, all single-grain ages were included in QTQt models. Although we routinely used the RDAAM and ZRDAAM radiation damage models (Flowers et al., 2009; Guenther et al., 2013) to model the age-eU spread, we did not apply the concept of inheritance envelopes (e.g., Guenther et al., 2015), because of the relatively low overall spread in (U-Th-Sm)/He ages and eU. Age-eU, age-ESR and age-Ft plots are included in Figure S1 in Supporting Information S1 and samples showing an age-eU and/or age-Ft trend are marked in Table 1.

3.4. Apatite Fission Track Thermochronology

Apatite fission track (AFT) thermochronology is based on the spontaneous fission of ^{238}U , which creates charged particles that form linear damage zones in the crystal lattice called fission tracks. Through quantification of fission tracks and the abundance of the remaining parent isotope in apatite, a cooling age is generated for the sample. The temperature interval between 60°C and 120°C marks the apatite partial annealing zone (APAZ)

Table 1
(U-Th-Sm)/He Ages for Apatite (AHe) and Zircon (ZHe)

Apatite (U-Th-Sm)/He data									
TB ^a	Sample	Aliquots ^b	Lithology	UTM N ^c	UTM E ^c	Z (m)	WM (Ma) ^d	SE (Ma) ^e	% ^f
1	AL5	3	PRC	265,330	7,407,390	3,732	9.0	0.4	3.9%
	AL6	4	PRC	264,129	7,406,152	3,509	6.9	0.5	6.8%
	AL7	4	PRC	263,544	7,405,230	3,306	11.7	0.6	5.1%
	AL8	4	CAM	262,789	7,405,469	3,112	35.7	2.6	7.3%
	AL9	3	ORD	262,168	7,404,701	2,820	10.0	0.1	1.2%
2	AL4 ^g	3	ORD	265,693	7,407,476	3,761	9.4	3.3	35.6%
3	LU1	5	PRC	268,703	7,390,777	4,142	9.8	1.1	11.2%
	AC1 ^g	3	PRC	269,588	7,386,416	4,123	7.7	0.4	5.5%
	TAC1	5	PIR	272,118	7,406,576	4,033	7.3	0.8	11.0%
	AC2	3	PRC	270,123	7,386,139	3,894	4.3	0.3	7.9%
	AL2	5	ORD	270,624	7,405,026	3,670	6.3	0.5	7.2%
	LU2	4	PRC	270,443	7,390,822	3,607	6.8	0.6	8.1%
4	MA3	3	SAB	272,520	7,398,204	3,863	6.4	0.4	6.6%
	AC6	5	BAL	272,000	7,384,350	3,769	3.5	0.2	4.6%
	AC3	4	CAM	270,778	7,385,071	3,574	4.1	0.8	19.4%
	MA2	4	ORD	274,321	7,397,718	3,477	5.1	0.6	11.1%
	LU5	3	ORD	274,792	7,391,378	3,415	6.3	0.4	5.7%
	LU4	3	ORD	273,074	7,392,891	3,385	5.2	0.8	15.5%
	LU6	3	SAB	275,647	7,391,245	3,297	4.2	0.2	5.7%
	LU7	4	SAB	277,533	7,391,911	3,263	3.4	0.3	7.3%
	LU3	4	SAB	271,736	7,393,079	3,220	3.5	0.3	7.5%
	LU9	3	ORD	283,558	7,390,518	2,787	4.1	0.3	6.1%
	LU12	4	ORA	289,357	7,386,938	2,375	3.5	0.4	10.3%
LU11	4	SAB	288,034	7,387,380	2,159	4.3	1.8	41.7%	
Zircon (U-Th-Sm)/He data									
TB ^a	Sample	Aliquots ^b	Lithology	UTM N ^c	UTM E ^c	Z (m)	WM (Ma) ^d	SE (Ma) ^e	% ^f
1	AL5	4	PRC	265,330	7,407,390	3,732	178.5	5.3	3.0%
	AL8 ^{g,h}	4	CAM	262,789	7,405,469	3,112	313.9	15.5	4.9%
2	AL3 ^g	3	PRC	270,128	7,405,319	3,631	27.0	1.9	6.9%
3	LU1	3	PRC	268,703	7,390,777	4,142	125.3	5.7	4.5%
	AC1 ^h	3	PRC	269,588	7,386,416	4,123	78.3	5.5	7.0%
	TAC1	6	PIR	272,118	7,406,576	4,033	339.2	62.6	18.5%
	MA1	2	CAM	271,055.1	7,399,705	3,960	50.6	1.1	2.2%
LU2 ^h	3	PRC	270,443	7,390,822	3,607	67.2	6.9	10.2%	

Table 1
Continued

Zircon (U-Th-Sm)/He data									
TB ^a	Sample	Aliquots ^b	Lithology	UTM N ^c	UTM E ^c	Z (m)	WM (Ma) ^d	SE (Ma) ^e	% ^f
4	AC6	5	BAL	272,000	7,384,350	3,769	415.4	35.7	8.6%
	LU4	5	ORD	273,074	7,392,891	3,385	153.6	13.1	8.5%
	LU3	4	SAB	271,736	7,393,079	3,220	314.7	23.7	7.5%
	LU9 ^h	3	ORD	283,558	7,390,518	2,787	110.6	10.7	9.7%

Note. Lithologies range from Puncoviscana Fm (PRC), Mesón Group (CAM), Santa Victoria Group (ORD), Pirgua (PIR), Balbuena (BAL) and Santa Bárbara (SAB) subgroups to Orán Group (ORA). Full (U-Th-Sm)/He data is provided in Table S1.

^aCorresponding tectonic block, for numbers see Figure 2. ^bNumber of aliquots used, excluding outliers. ^cUTM zone 20K. ^dWeighted mean age calculated in IsoplotR, excluding outliers. ^eStandard error (1σ) of the weighted mean age. ^fPercentage of SE of the weighted mean age. ^gSamples with age-Ft relationship. ^hSamples with age-eU relationship.

(Wagner et al., 1989) in which tracks can be partially annealed. The exact temperature interval of the APAZ varies with cooling rate and kinetic characteristics, which can be quantified using the diameter of the etch pits (Carlson et al., 1999; Donelick, 1993; Donelick et al., 1999; Ketcham et al., 1999).

We analyzed 19 samples for AFT thermochronology using the external detector method (Gleadow, 1981). The sample fraction containing apatites ($2.96 < \rho < 3.3 \text{ g/cm}^3$) was mounted on a glass slide with epoxy, ground and polished. Apatite mounts were then etched using 5.5 N HNO₃ at 21°C for 20 s (Donelick, 2005), packed with a mica detector on top and sent to Oregon State University for thermal neutron irradiation. After irradiation, the mica detectors were etched in 40% HF at 21°C for 45 min.

All samples were analyzed at the University of Potsdam using a Leica DMRM microscope at 1,250X magnification and the FTStage software (Dumitru, 1994). For calculation of AFT ages a zeta correction factor (Hurford & Green, 1983) of 380.5 ± 7.5 (WvK) was applied. We measured the diameter of the etch pits *Dpar* (Donelick, 2005; Sobel & Seward, 2010) as a proxy for kinetic characteristics of the crystal, which strongly influence annealing (Barbarand et al., 2003; Carlson et al., 1999; Ketcham et al., 1999). *Dpar* measurements were calibrated by correlating individual *Dpar* measurements for Fish Canyon Tuff and Durango apatite with those by Donelick et al. (1999), yielding a correction factor of 1.07. For the full calibration procedure see Sobel and Seward (2010). It was not possible to measure a statistically relevant number of track-in-track (TINT) lengths. Although due to the low number of spontaneous track measurements (N_s), the sample size according to standard criteria (Yates et al., 1999) was too small for calculating viable chi-square statistics, we performed a chi-square test of independence on all samples. For samples that passed the chi-square test ($P(\chi^2) > 5\%$), we calculated a pooled age and one sigma error (Galbraith & Laslett, 1993); for samples that exhibited multiple age components and thus did not pass, we calculated a central age in IsoplotR. These samples were also checked for a possible correlation between *Dpar* and single-grain ages, which would explain larger-than-normal age scatter. Non-passing samples were generally excluded from modeling procedures. AFT data is summarized below (Table 2). Radial plots from RadialPlotter (Vermeesch, 2009) can be found in Figure S2 (Supporting Information S1).

3.5. QTQt Modeling

To better constrain pre-Cretaceous and Andean phases of exhumation we conducted thermal modeling in the QTQt software v5.8.0 (Gallagher, 2021) using data from Tables 1 and 2. This software is able to take into account kinematic characteristics of single-grain ages. AHe and ZHe samples exclude outliers as discussed above. For AHe samples, we used the radiation damage model of Flowers et al. (2009). For ZHe samples, we used the radiation damage model of Guenther et al. (2013). For one ZHe sample (TAC1), where an inheritance component was considered, we modeled ZHe age populations as two separate samples. The annealing model of Ketcham et al. (2007) was used for AFT samples. AFT data also included mean *Dpar* measurements to implement compositional control in the models.

Models were run for single tectonic blocks, because QTQt currently does not allow for a tectonic offset in the thermal history modeling. We modeled spatially offset elevation profiles separately, because the lateral offset and the presence of faults between W-E elevation profiles disrupt age-elevation or age-stratigraphy relationships. Furthermore, samples located at the leeward side of the Tilcara Range were modeled separately from samples

Table 2
Apatite Fission Track Data^a

TB ^b	Sample	Lithology	UTM N ^c	UTM E ^c	Z (m)	N ^d	Ns	Ni	Nd	RhoS (x10 ⁵)	RhoI (x10 ⁵)	RhoD (x10 ⁵) ^e	Age (Ma) ^f	±1σ (Ma)	P(χ ²) (%) ^g	Dpar (μm) ^h	SD (μm) ⁱ
1	AL5	PRC	265,330	7,407,390	3,732	17	44	708	4,076	10.746	172.906	9.924	11.7	1.8	61.1%	2.5	0.3
	AL6	PRC	264,129	7,406,152	3,509	10	72	1,427	4,076	24.454	484.667	9.879	9.5	1.2	31.6%	2.6	0.2
	AL7	PRC	263,544	7,405,230	3,306	10	27	455	4,076	9.080	153.016	9.849	11.1	2.2	73.5%	2.1	0.2
	AL9	ORD	262,168	7,404,701	2,820	16	178	3,132	4,076	24.087	423.818	9.820	10.6	0.8	55.4%	2.3	0.3
2	AL3	PRC	270,128	7,405,319	3,631	20	41	633	4,076	7.417	114.511	9.984	12.3	2.0	97.7%	2.3	0.7
3	AC1	PRC	269,588	7,386,416	4,123	13	49	978	4,076	12.259	244.670	10.164	9.7	1.4	27.2%	2.3	0.3
	AC2	PRC	270,123	7,386,139	3,894	12	36	911	4,076	8.607	217.815	10.119	7.6	1.3	80.9%	2.3	0.2
	AL2	ORD	270,624	7,405,026	3,670	15	56	1,087	4,076	17.950	348.422	10.029	9.8	1.4	30.6%	2.6	0.2
	LU2	PRC	270,443	7,390,822	3,607	15	58	1,346	5,187	9.028	209.501	12.904	10.6	1.4	76.5%	2.3	0.2
4	AC3	CAM	270,778	7,385,071	3,574	12	38	914	4,076	12.335	296.678	10.089	9.2	1.9	2.4%	2.4	0.2
	AC6	BAL	272,000	7,384,350	3,769	12	39	1,284	4,076	7.477	246.172	10.059	6.9	1.6	1.1%	2.4	0.3
	LU12	ORA	289,357	7,386,938	2,375	26	171	1,242	5,187	11.404	82.831	12.517	32.7	2.7	30.7%	3.2	0.5
	LU3	SAB	271,736	7,393,079	3,220	15	34	782	5,187	8.569	197.078	12.839	10.6	1.9	92.5%	2.3	0.4
	LU4	ORD	273,074	7,392,891	3,385	16	37	1,503	5,187	8.286	336.605	12.796	6.0	1.0	64.0%	2.3	0.3
	LU5	ORD	274,792	7,391,378	3,415	21	66	2,328	5,187	11.080	390.812	12.753	6.9	0.9	88.8%	2.4	0.2
	LU6	SAB	275,647	7,391,245	3,297	9	39	1,629	5,187	6.173	257.853	12.710	5.8	0.9	82.2%	2.6	0.3
	LU7	SAB	277,533	7,391,911	3,263	5	12	381	5,187	5.889	186.984	12.646	7.6	2.2	78.9%	2.3	0.3
	LU9	ORD	283,558	7,390,518	2,787	17	111	4,034	5,187	8.528	309.943	12.582	8.3	1.6	0.0%	2.4	0.2
	MA2	ORD	274,321	7,397,718	3,477	7	10	206	5,187	8.692	179.065	12.432	11.5	3.7	32.7%	2.6	0.5

Note. For lithology abbreviations see caption of Table 1.

^aζ = 380.5 ± 7.5. ^bCorresponding tectonic block, for numbers see Figure 2. ^cUTM zone 20K. ^dNumber of individual crystals dated. ^eCN5 standard glasses monitored thermal neutron fluences. ^fCentral age for samples that did not pass chi-square test, pooled age for all other samples. ^gP(χ²) (%) is the chi-square probability (Galbraith & Laslett, 1993; Green, 1981). ^hCorrected Dpar calculated after Sobel and Seward (2010). ⁱStandard deviation of measured Dpars.

located at the windward side, because post-3 Ma denudation rates indicate a strong erosional gradient across the Tilcara Range (Pingel et al., 2019; see section 2.1) that might have affected pre-3 Ma cooling rates. For models run using age-elevation relationships (Table 3), we used the sampling elevation as input. For models using age-stratigraphy relationships, we calculated a “stratigraphic elevation” relative to the stratigraphically deepest sample by projecting samples onto cross-sections. We then measured the stratigraphic offset between samples, using the basement-Salta Group unconformity as a zero offset line. The resulting values were normalized, so that the stratigraphically deepest sample is located at zero m pseudo-elevation. This correction was conducted separately for all three sections, to account for irregularities in unit thicknesses within the Tilcara Range and San Lucas block. In cases where the basement-Salta Group unconformity has been eroded, the base of the Mesón Group was used as a zero offset line. Furthermore, variations in burial depth due to varying thickness of Cenozoic strata and erosion of basement strata before deposition of the Salta Group have not been taken into account.

Models were consistently run with ≥100,000 repetitions post burn-in, to ensure strong likelihood and posterior chains. In cases where 100,000 iterations was an insufficiently large sampling size, we increased the number of iterations to 200,000 (Table 3). AFT-only models were regularly run with 200,000 iterations because of the increase in model fit with comparatively low extra computing time. We used a maximum bounding box of 275 ± 275 Ma and 70 ± 70°C, 80 ± 80°C or 150 ± 150°C (AHe, AFT, and ZHe models, respectively). Present day temperature offset of the samples was set to a maximum of 10 ± 10°C, because all samples were at the surface when sampled. Additional time-temperature constraints based on when the samples were at the surface are documented in Table 3. In all cases, we present the expected model, which is a weighted mean model using the posterior probability for weighting. See Gallagher et al. (2009) for further information. A complete summary of QTQt models and their respective parameters and constraints is given in Table 3. Models that are not discussed in detail in the results section can be found in Figure S3 (Supporting Information S1).

Table 3
QTQt Modeling Parameters and Constraints (Stratigraphic and Sample Constraints)

General constraints									
Modeling interval ^a	0–550 Ma, 0–300°C		Maximum cooling rate			1,000°C/Ma			
eU resampling	No		Reheating			Allowed			
Iterations ^b	≥100,000/≥100,000		Gradient variation			Allowed			
Present day offset ^c	≤10 ± 10°C		Surface temperature			10 ± 10°C			
Model-specific constraints									
Run	Stratigraphic constraints		Sample constraints				Offset (°C) ^e	Iterations	
	Time (Ma)	Temp. (°C)	AHe	AFT	ZHe	Trend ^d			
5a	500 ± 50	0–20			AL3	S	35.01	200,000	
	510 ± 30	0–20			AL5 AL8				
5b	500 ± 50	0–20		AL5		E	27.36	200,000	
	465 ± 20	0–20		AL7 AL9					
5c	500 ± 50	0–20	AL5			S	24.21	100,000	
	510 ± 30	0–20	AL6						
	465 ± 20	0–20	AL7 AL8 AL9						
5d	500 ± 50	0–20			AL3	S	36.81	100,000	
	510 ± 30	0–20	AL5		AL5				
	465 ± 20	0–20	AL6 AL7 AL8 AL9		AL7				
									AL8
									AL9
5e	500 ± 50	0–20		AL5	AL5	E	27.36	100,000	
	510 ± 30	0–20		AL7					
	465 ± 20	0–20		AL9					
6a	510 ± 30	0–20			MA1	E	2.19	100,000	
	115 ± 15	0–20			TAC1				
6b	465 ± 20	0–20	AL2			E	10.89	100,000	
	115 ± 15	0–20	TAC1						
6c	465 ± 20	0–20	MA2			E	11.58	100,000	
	60 ± 2	0–20	MA3						
6d	465 ± 20	0–20	AL2			E	16.68	100,000	
	115 ± 15	0–20	MA2						
	60 ± 2	0–20	MA3 TAC1						
6e	465 ± 20	0–20		AL2		E	–	200,000	
6f	465 ± 20	0–20		MA2		E	–	200,000	
6g	510 ± 30	0–20	AL2	AL2		E	10.89	100,000	
	465 ± 20	0–20			MA1				
	115 ± 15	0–20	TAC1		TAC1				

Table 3
Continued

Model-specific constraints								
Run	Stratigraphic constraints		Sample constraints				Offset (°C) ^e	Iterations
	Time (Ma)	Temp. (°C)	AHe	AFT	ZHe	Trend ^d		
6h	465 ± 20	0–20	MA2	MA2		E	11.58	100,000
	60 ± 2	0–20	MA3					
7a	500 ± 50	0–20			LU1	S	48.21	100,000
7b	465 ± 20	0–20			LU2	E	17.94	100,000
					LU4			
7c	465 ± 20	0–20			LU9	S	27.99	100,000
					LU4			
7d	500 ± 50	0–20	LU1			E	27.66	100,000
			LU2					
7e	500 ± 50	0–20	LU3				16.05	100,000
			LU4					
			LU5					
			LU6					
			LU7					
			LU1					
			LU2					
7f	465 ± 20	0–20	LU9			E	18.84	200,000
			LU11					
			LU12					
7g	500 ± 50	0–20		LU2		E	–	200,000
7h	465 ± 20	0–20			LU3	S	84.87	200,000
					LU4			
					LU5			
					LU6			
					LU7			
					LU12			
7i	500 ± 50	0–20	LU1		LU1	E	16.05	100,000
			LU2		LU2			
7j	465 ± 20	0–20			LU3	S	116.55	100,000
					LU4			
					LU5			
					LU6			
					LU7			
7k	465 ± 20	0–20			LU9	E	18.84	200,000
					LU11			
					LU12			
					LU12			

Table 3
Continued

Model-specific constraints								
Run	Stratigraphic constraints		Sample constraints				Offset (°C) ^e	Iterations
	Time (Ma)	Temp. (°C)	AHe	AFT	ZHe	Trend ^d		
8a	500 ± 50	0–20	AC1			E	16.47	100,000
	510 ± 30	0–20	AC2					
	70 ± 2	0–20	AC3					
			AC6					
8b	500 ± 50	0–20	AC1			E	6.87	100,000
			AC2					
8c	510 ± 30	0–20	AC3			E	5.85	100,000
	70 ± 2	0–20	AC6					
8d	500 ± 50	0–20		AC1		E	6.87	200,000
				AC2				
8e	500 ± 50	0–20		AC1		S	17.82	200,000
				AC2				
8f	500 ± 50	0–20	AC1	AC1	AC1	E	16.47	100,000
	510 ± 30	0–20	AC2	AC2				
	70 ± 2	0–20	AC3					
			AC6					
8g	500 ± 50	0–20	AC1	AC1	AC1	E	6.87	100,000
			AC2	AC2				
8h	500 ± 50	0–20		AC1	AC1	S	17.82	100,000
				AC2				

Note. Stratigraphic constraints describe broad time-temperature conditions at which the included samples were at the surface and are used as additional modeling constraints. Sample constraints describe the samples, low-temperature thermochronology methods and trends (age-elevation or age-stratigraphy, see Figure 4) included in the corresponding model.

^aTemperature interval for AHe-, AFT-, and ZHe-only models 0–140°C, 0–160°C, and 0–300°C, respectively. ^bNumber of iterations burn-in and post-burn-in. ^cPresent-day offset maximum 10 ± 10°C, unless original offset was lower. ^dAge-elevation (E) or age-stratigraphy (S). ^eThermal offset between the hottest and coldest sample, based on a geothermal gradient of 30°C/km.

4. Results

4.1. Field Geology

From west to east, the study area is divided into four tectonic blocks (TB1–TB4), of which TB1–TB3 are located within the Tilcara Range and TB4 (San Lucas block) encompasses the area east of the Tilcara Range Frontal Fault. TB1 to TB3 consist of mostly Precambrian to Ordovician basement rocks that generally dip to the WSW–WNW (Figure 2). We found large domains of upper Cambrian–lower Ordovician rocks, identified by their characteristic lithological assemblage, fossils and trace fossils. Discrepancies between existing maps (e.g., González & Tchilinguirian, 2003; Rodríguez-Fernández et al., 1999) can be explained by the improved accessibility of the Tilcara Range outcrops along newly-built roads, the increasing quality of satellite imagery used for interpolation of formation boundaries and the large-scale character of the aforementioned maps. Both the Puncoviscana Formation and Santa Victoria Group show a strong lithological contrast to the intervening Mesón Group. This contrast is further accentuated by the Tilcaric unconformity, which is strongly angular near Huacalera. The alternating lithologies in the Puncoviscana Formation and Santa Victoria Group allowed the accommodation of intensive small-scale folding in these units (Figures 2 and 3a). In contrast, the competent sandstones and quartzites of the Mesón Group are less deformed and form excellent markers for large-scale deformation in the basement blocks of the Tilcara Range. Within the Tilcara Range there are also small, locally restricted outcrops of the Pirgua Subgroup (see also Kley et al., 2005).

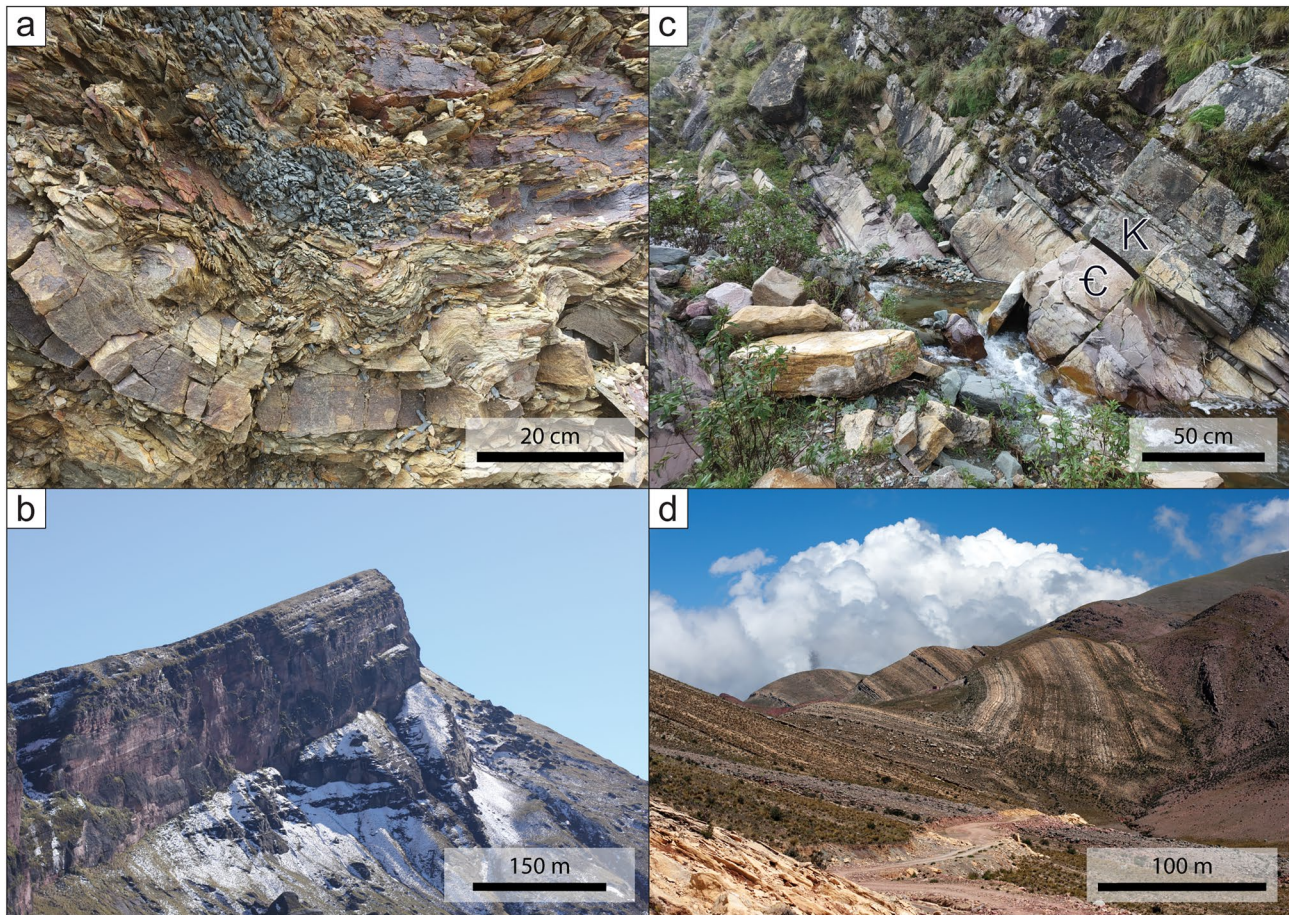


Figure 3. (a) Small-scale folding in the Santa Victoria Group east of Alonso. Due to alternating competent and incompetent lithologies, the Santa Victoria Group strata can easily accommodate strain. (b) Angular unconformity (30°) between the Santa Victoria Group and the Cretaceous Pirgua Subgroup at Quebrada Amarilla. (c) Paraconformity between the Mesón Group and the Cretaceous-Paleogene Yacoraite Formation near Las Animas. (d) Footwall syncline in the Cretaceous-Paleogene succession. The Yacoraite Formation and Pirgua Subgroup show an overturned western limb.

NW-SE striking high-angle faults divide TB1–TB3 internally, as seen from offsets within the Precambrian to Ordovician basement. In some cases, they show an apparent strike-slip movement, as indicated in Figure 2a. Kley et al. (2005) suggest that these apparent strike-slip faults within the basement blocks of the Tilcara Range are in fact Cretaceous normal faults that were tilted during block rotation linked to fault activity along NNE-SSW striking reverse faults. Evidence supporting this is found within TB3, where one of the faults cuts off syn-rift strata of the Pirgua Subgroup against upper Cambrian-lower Ordovician rocks, suggesting a half-graben setting. The syn-rift strata consist of locally confined, proximal breccia grading into conglomerates and cross-bedded sandstones that unconformably overlie the Santa Victoria Group.

The tectonic blocks of the Tilcara Range are tilted along and separated by NNE-SSW high-angle, east-vergent reverse faults (Figure 2c, Alonso transect), recognized also by previous authors (Alonso et al., 2012; González & Tchilinguirian, 2003; Rodríguez-Fernández et al., 1999). A minor reverse fault with a similar orientation occurs west of Alonso (Figure 2a) and accommodates shortening within TB2. These faults appear to cut NW-SE striking faults (Figure 2a), suggesting that the most recent Andean shortening was accommodated by thrusting along the NNE-SSW fault system. Although we can only speculate about its timing and mechanism of formation, the existence of approximately north-striking, east-vergent Paleozoic reverse faults that have been reactivated during Andean shortening has been proven in the Eastern Cordillera and specifically within the Tilcara Range (e.g., Barrabino et al., 2015). The NNE-SSW striking fault system continues up to the Tilcara Range Frontal Fault, which marks a transition in structural elevation and outcropping lithologies,

and forms the boundary between the Tilcara Range and the San Lucas block. A direct fault contact between basement strata of the Tilcara Range and syn-rift strata of the San Lucas block (Figure 2a) is not visible in the field, but the fault is causally linked to the formation of a close (interlimb angle $\sim 35^\circ$), east-verging footwall syncline within the Salta Group of the San Lucas block, which can be traced along the Tilcara Range Frontal Fault for several kilometers (Figure 2a). The western limb of this syncline bordering the reverse fault has been overturned (Figure 2c, Alonso and Las Animas transect). Similar folds showing an identical NE-SW to NNE-SSW strike can be observed farther east, suggesting the presence of possibly blind reverse or thrust faults within TB4 (Figure 2c, San Lucas transect). Toward the east, the Salta Group and the overlying Orán Group form increasingly open, upright folds. The presence of the Lumbreira Formation, with a middle-late Eocene depositional age known from the vertebrates fossil record assigned to the Riochican-Casamayoran (Pascual et al., 1981) and U-Pb dating of a tuff layer near its top (Del Papa et al., 2010), within the synclines shows that fault activity along the Tilcara Range Frontal Fault, and in general shortening within the San Lucas block, must be younger than the late Eocene.

Within the Tilcara Range, most of the Salta Group has been eroded and is only present in small outcrops related to synclines. In contrast, east of the Tilcara Range Frontal Fault, a full succession of the Salta Group is preserved, from basal conglomerates of the Pírgua Subgroup to the transition of the Santa Bárbara Subgroup into the overlying Orán Group close to San Lucas. Both in the northern and middle part of the area, the Pírgua Subgroup unconformably overlies the Santa Victoria Group (Figure 2a). In the north, we observed a strong angular unconformity (30° , Figure 3b), whereas at Huairahuasi the angle is significantly smaller ($<11^\circ$). We attribute this angular variety to folding of the Santa Victoria Group before deposition of the Salta Group, also shown in other locations within the Eastern Cordillera (e.g., Alonso et al., 2012). Short wavelength folding is also clear from rapidly changing bedding orientations within the Puncoviscana Formation and Santa Victoria Group (Figure 2). However, large-scale folding with NE-SW to NNE-SSW striking fold axes also occurs in the Santa Victoria Group (Figure 2a), suggesting that Andean deformation has affected these rocks as well as the Salta Group strata.

The thickness of the Salta Group varies from north to south and west to east, largely controlled by the thickness changes of the Pírgua Subgroup. Transects in Figure 2c and sections from Boll et al. (1989) 5 km south of the Alonso transect, document a rapidly decreasing thickness of the Pírgua Subgroup from 413 m in the north to 10 m at Huairahuasi (compare sections in Figure 2c). South and east of Huairahuasi, the Pírgua Subgroup is not preserved, leaving the Yacoraite Formation resting paraconformably on top of the Mesón and Santa Victoria Groups (Figure 3c) near Las Animas and San Lucas. Although the Balbuena Subgroup retains a relatively stable thickness from north to south and west to east, the thickness of the Santa Bárbara Subgroups varies from >487 m in the north (Boll et al., 1989) to >206 m in the south and >650 m in the west to 492 m in the east. The latter strongly contrasts with the measured thickness of >198.8 m at the Rio San Lucas by Boll et al. (1989).

The relatively large thickness of the Pírgua Subgroup north of Quebrada Amarilla, its rapid thinning toward the south and the presence of breccias and proximal conglomerate levels at its base suggest the presence of a remnant NW-SE striking Cretaceous normal fault north of Quebrada Amarilla, compatible with the data of Kley et al. (2005). Combined with locally confined and fault-bound outcrops of syn-rift strata within the Tilcara Range, this supports the general idea that at the margins of the Lomas de Olmedo sub-basin, the thickness of the Pírgua Subgroup varies dramatically due to its deposition in local half-graben settings (Marquillas et al., 2005; Salfity & Marquillas, 1994).

4.2. Thermochronology

Thermochronological data were plotted in age-elevation and age-stratigraphy diagrams to analyze trends (Figure 4). We calculated regression lines using a linear fit based on weighted mean cooling ages that exclude outliers. Visual guides were traced by hand (Figure 4, dashed lines) whenever sample statistics were not robust enough to calculate a fit (i.e., for trends with only two samples or for samples with high dispersion), but visually a trend could be seen. AHe ages range from 1.7 ± 0.5 Ma to 43.5 ± 1.8 Ma (excluding one outlier) and show a decrease from west to east, concordant with sampling elevation (Figure 4 and S1). AHe ages at the leeward side of the Tilcara Range are generally older than ages at similar elevations at the windward side. Within coherent NW-SE transects, there is a pervasive positive age-elevation trend across the Tilcara Range Frontal

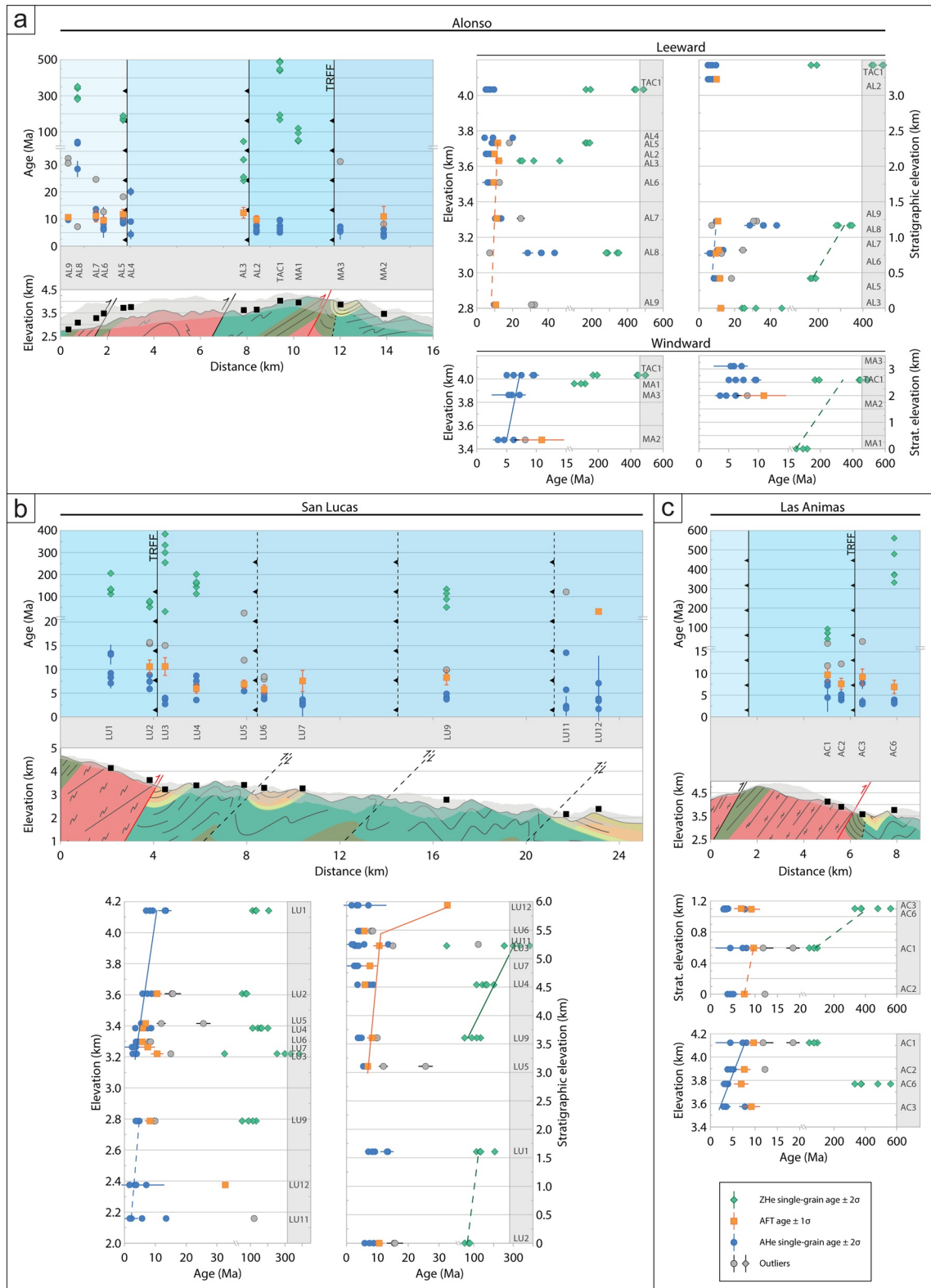


Figure 4. Diagrams of the (a) Alonso transect, (b) San Lucas transect, and (c) Las Animas transect showing single-grain AHe and ZHe ages, as well as AFT ages plotted against the distance along the section. Schematic geological sections (see also Figure 2c) with swath profiles show the location and elevation of the samples. Samples are projected onto the section and the location of faults and formation boundaries are drawn relative to the samples. Transects are accompanied by age-elevation and age-stratigraphy plots, including calculated regression lines (solid) and visual guides (dashed). Note the breaks in the y- and x-axes.

Fault (Figure 4), indicating a lack of significant fault activity after exhumation beyond the APRZ. Within the AL9-AL5 vertical profile of TB1, AHe ages range from 43.5 ± 1.8 Ma to 8.4 ± 0.2 Ma and show a disperse but positive age-stratigraphy trend (Figure 4a). Assuming the lower, stratigraphically younger samples were only partially reset, this could explain the increasingly scattered ages in these samples. Similarly, the overdispersion of single-grain AHe ages within sample AL4 (TB2) could be caused by partial resetting. However, fully reset AFT ages and burial of the samples to >4.5 km (see e.g., Siks & Horton, 2011) suggest that AHe ages should be fully reset. For sample AL4, an age-ESR trend could provide an alternative explanation for dispersion, but the small absolute difference in ESR and rapid exhumation also make this an unlikely solution. AHe ages show no offset across faults and between TB2 and TB3 there is a positive age-elevation trend. Within the San Lucas transect, samples LU1-LU7 and LU9-LU12 form continuous age-elevation trends, although the latter shows a slight offset toward older ages. This might suggest that minor thrust or reverse faults disturb the basement strata internally. In theory, partial resetting of AHe cooling ages could also explain a deviation from the general age-elevation trend. However, the samples show late Miocene to Pleistocene cooling ages, whereas the depositional ages of the source rocks range from the upper Cambrian to the Miocene. Furthermore, samples LU9-LU12 show a continuous age-elevation trend with a similar slope as the trend seen in samples LU1-LU7.

AFT ages range from 5.8 ± 0.9 Ma to 12.3 ± 2.0 Ma for reset ages. Coinciding with the AHe age distribution, spatial relationships between samples are disrupted within tectonic blocks. We attribute this to disruption of the age pattern due to fault activity and propagation of fault activity from north to south. AFT ages from the leeward side show a positive, near-vertical age-elevation trend, contrasting with the negative trend seen in the AHe data (Figure 4a). Again, there is no evidence for fault activity between the tectonic blocks, suggesting that late Miocene exhumation of these fault blocks occurred homogeneously and fault activity along the NNE-SSW fault system ceased before exhumation through the APAZ.

At the windward side of the Tilcara Range, AFT cooling ages do not show a general age-elevation trend, contrary to the AHe data (Figure 4). Instead, the samples adhere to an overall positive age-stratigraphy trend (Figure 4 and S1). We attribute the lack of an age-elevation relationship to the interplay of both absolute sampling elevation and Cenozoic burial depth, and suggest that the majority of folding and faulting within TB4 must have taken place after cooling through the APAZ, placing an important constraint on deformation in this block. The stratigraphically highest sample LU12 has an age of 32.7 ± 2.7 Ma: this comparatively old age likely results from the limited thickness of foreland strata to the east, which cannot have buried the sample deeply enough to cause resetting prior to a Miocene-Pliocene exhumation event. Several samples from the Santa Bárbara Subgroup also show ages that are older than expected for the general age-stratigraphy trend and might only be partially reset. AFT ages show a subtle age offset across the Tilcara Range Frontal Fault in all three transects, with slightly younger ages in the hanging wall (Figure 4). The minor offset indicates that fault-related exhumation beyond the APAZ was limited.

ZHe ages range from 24.1 ± 0.2 Ma to 560.8 ± 10.0 Ma (excluding one young and one old outlier). The highest sample in TB3 within the Alonso transect shows two age populations: one Early-Middle Jurassic and one late Cambrian-early Silurian. We cannot exclude either of these based on ICP-MS data, grain geometry or intragrain impurities and there is no age-eU or age-Ft relationship. Because both populations are older than the Cretaceous depositional age, we argue that the sample is partially reset and that the ZHe ages show an age distribution that reflects the detrital provenance—and as such the radiation damage history—of the single aliquots. ZHe single-grain ages do not show an overall age-elevation trend, nor an overall age-eU trend (Figure S1 in Supporting Information S1). However, within TB1, ZHe samples show a positive age-stratigraphy trend, similar to the AHe data. Within TB4, there is a positive age-elevation and/or age-stratigraphy trend, neither confirming nor rejecting the hypothesis that deformation in this block took place after cooling beyond the APAZ. The sample LU3 shows ZHe ages that are older than its depositional age (Figure 4b), and was not fully reset. Similar to sample LU3, the TB4 sample in the Las Animas transect is non-reset and reflects detrital provenance rather than Paleogene exhumation. Since sample LU3 fits only on an age-stratigraphy trend (Figure 4b) it is likely that deformation took place after cooling through the ZPRZ.

ZHe samples were collected from both sides of the reverse faults dividing the tectonic blocks (Figure 4). Although from TB2 to TB3, ages appear to be offset (Figure 4a), age-elevation plots across the fault show that there is a continuous positive age-elevation trend from TB2 to TB3. Within the windward side of the Tilcara Range, ZHe

data across the Tilcara Range Frontal Fault show a clear offset toward younger ages in the hanging wall block (Figures 4b and 4c), indicating that there has been fault activity after the samples cooled through the ZPRZ.

4.3. QTQt Modeling

Based on the different trends for AHe, AFT and ZHe samples described above, we initially created single-method QTQt models. Depending on the trend seen in the thermochronological data (Figure 4), models were run in age-elevation and/or age-stratigraphy space. Age-elevation models use the sampling elevation, whereas age-stratigraphy models use the stratigraphic pseudo-elevation of samples, measured from the cross-sections in Figure 2c (see section 3.5 for full methodology). Age-elevation models are based on the assumption that deformation processes, which change spatial relationships between samples, terminated before cooling through the APRZ, APAZ or ZPRZ. In contrast, age-stratigraphy models assume deformation has not yet occurred. Single-method models (see Figure S3 in Supporting Information S1) that showed robust results were combined into multi-method models, which were preferably used for interpretation of thermal histories (Figures 5–8). For age-elevation (age-stratigraphy) models where single-grain ages of one method are incompatible with an age-elevation (age-stratigraphy) trend, we still used at least one sample of that method to impose better time and temperature constraint. Cooling rates are calculated from the visual inflection points of the hot sample 95% confidence interval, obtaining a lowest and highest cooling rate for the most recent exhumation phase. We report these as average cooling rates with standard deviation.

4.3.1. Alonso Transect (Leeward)

Early exhumation within TB1 and TB2 is constrained by a multi-sample age-stratigraphy ZHe model (model 5a, Figure S3 in Supporting Information S1) that we modeled following the age-stratigraphy relationship seen in Figure 4a. Predicted ZHe ages are generally slightly older than observed ages. Although the model suggests an early, pre-Salta Group exhumation of the Tilcara Range between the Carboniferous and the Early Cretaceous (330–140 Ma), ZHe ages cannot constrain the Miocene-Pliocene exhumation well, suggesting an onset of exhumation between 16 and 2 Ma.

Andean exhumation is constrained by single- and multi-method models using AHe and AFT samples. An age-elevation AFT model for TB1 (model 5b, Figure 5b; see also Figure 4a), shows an onset of rapid exhumation between 24 and 16 Ma. In contrast, an AHe model for TB1 (model 5c, Figure S3 in Supporting Information S1) using an age-stratigraphy relationship (see also Figure 4a) proposes an early, Cretaceous exhumation with an onset between 135 and 114 Ma, as well as a Miocene exhumation starting between 13 and 10 Ma with a decreasing exhumation rate <9 Ma. For both models, predicted ages show a fairly good fit with the observed ages. The discrepancy in the onset of exhumation between the models can be explained by the different temperature intervals that AHe and AFT cooling ages document. As such, AFT ages are better suited to document early cooling and the earliest onset of exhumation.

We ran one multi-method age-stratigraphy model (model 5d, Figure 5c) for TB1 and TB2, using five AHe, one AFT and three ZHe ages. The model shows an early pulse of exhumation from the Mississippian to the Early Jurassic (335–200 Ma), which is roughly within the timeframe given by model 5a. The samples were re-buried below the APAZ between 245 and 26 Ma. Late Oligocene to Miocene exhumation is well-constrained in this model and started at approximately 26 Ma, slightly earlier than in model 5b. An age-elevation model for TB1 (model 5e, Figure 5d) that excludes AHe ages shows Andean rapid exhumation starting in the early Miocene (21–16 Ma) and slowing down in the middle Miocene (13–12 Ma). Although both multi-sample models agree on a late Oligocene to middle Miocene (26–16 Ma) onset of rapid exhumation, model 5d shows a much tighter constraint on the timing of exhumation, which could also be connected to the larger number of samples modeled. Furthermore, observed ages are more in accordance with predicted ages in model 5d, suggesting a higher reliability.

4.3.2. Alonso Transect (Windward)

Pre-Cretaceous exhumation of the windward side of the Tilcara Range is constrained by a ZHe model for TB3 (model 6a, Figure S3 in Supporting Information S1). Samples were modeled in age-elevation space, based on the small amount of internal deformation of TB3 after the onset of cooling. Predicted ages match the observed ages well. The model shows an early exhumation from the Late Jurassic to the Early Cretaceous (150–117 Ma) to bring

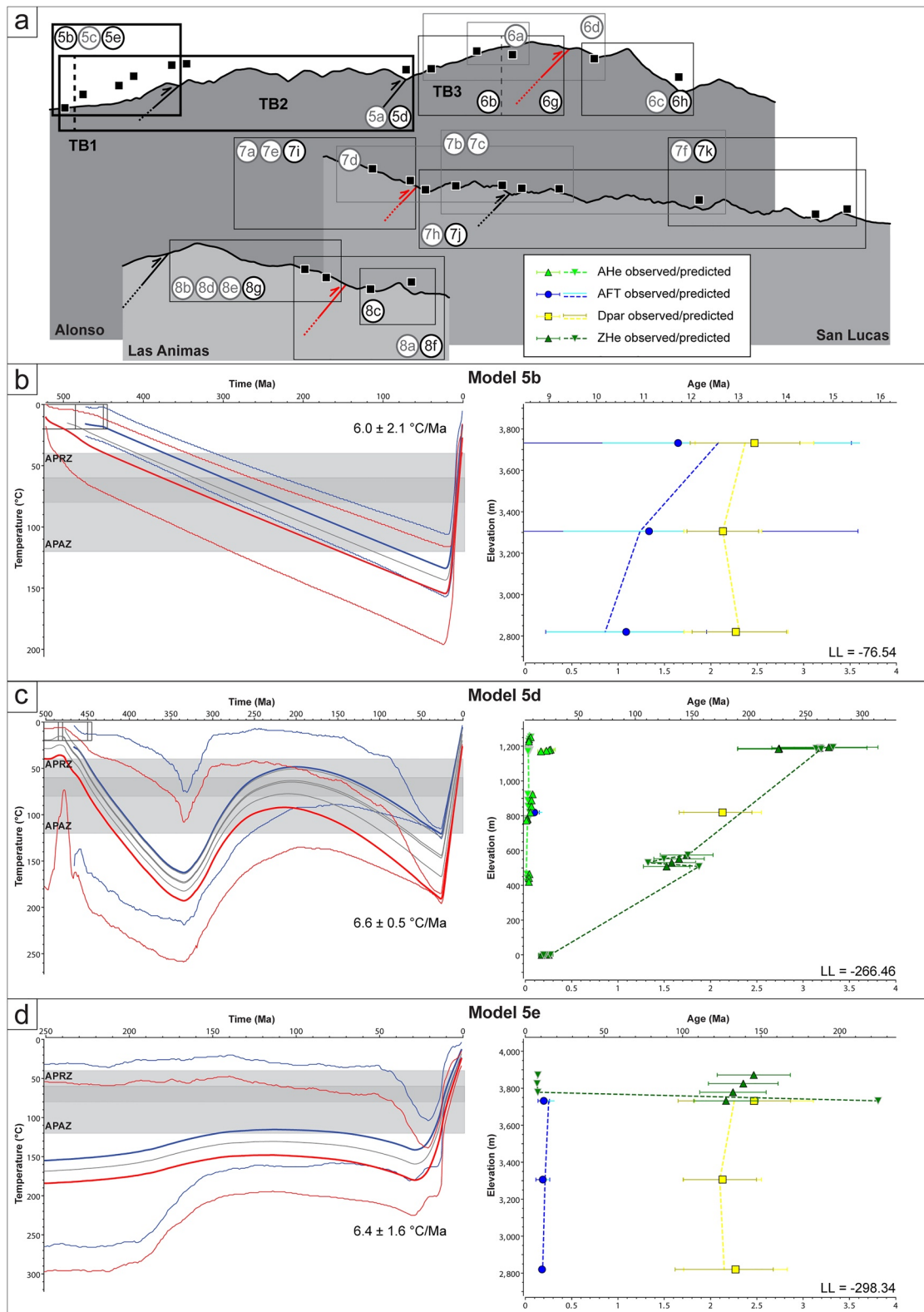


Figure 5. Modeling results for the leeward side of the Alonso section. (a) Shows the subset of samples used for individual models (see also Table 3) and its location on the section. Models marked in gray are shown in Figure S3 in Supporting Information S1. The Tilcara Range Frontal Fault is marked in red. Models (b) 5b, (c) 5d and (d) 5e are shown as the expected t-T-path and 95% confidence interval of the hot and cold sample. Average cooling rates with standard deviation are shown for the most recent exhumation phase. All models show the predicted and observed single-aliquot ages and the log likelihood (LL) to the right.

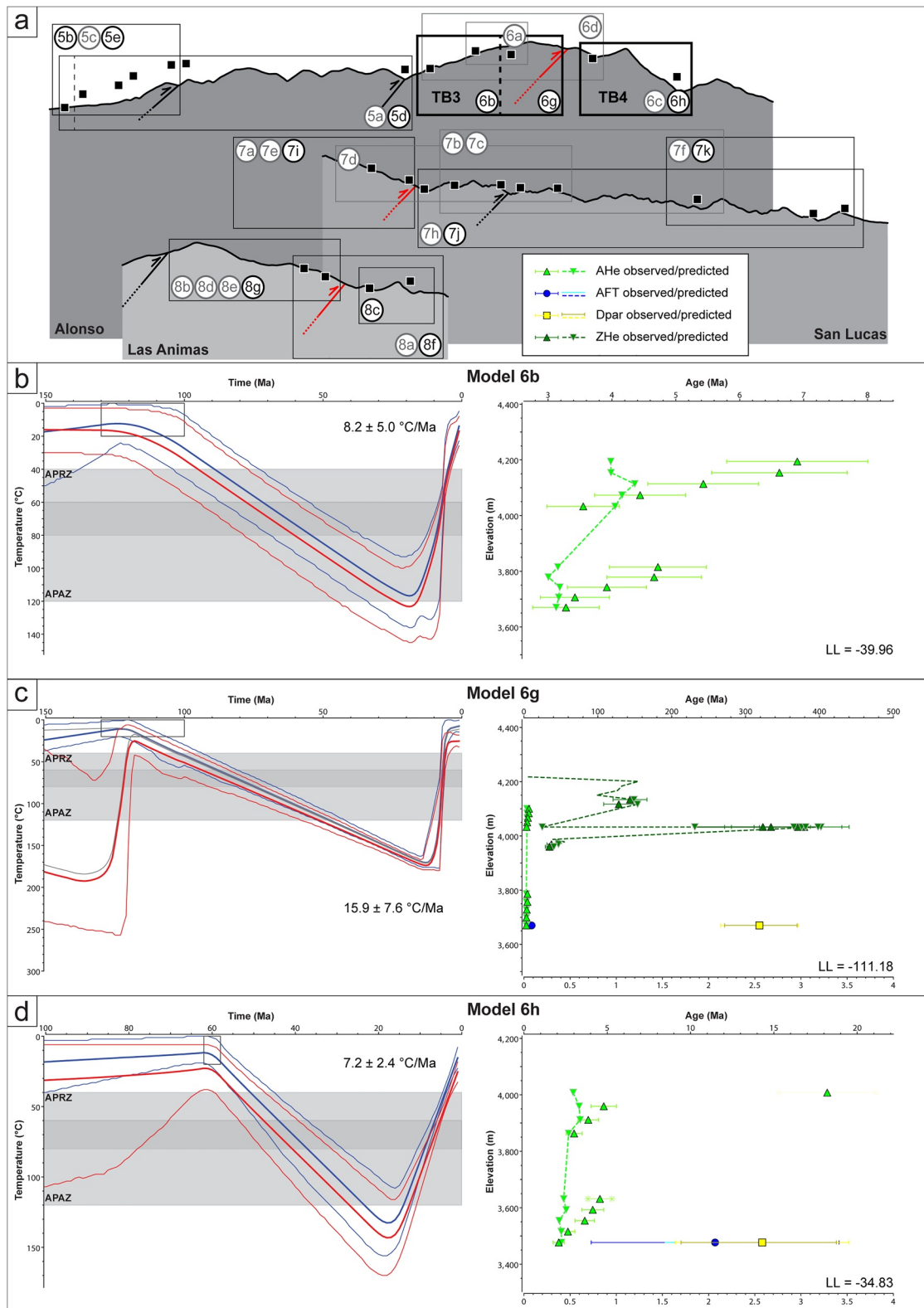


Figure 6. Modeling results for the windward side of the Alonso section. (a) Shows the subset of samples used for individual models (see also Table 3) and its location on the section. Models marked in gray are shown in Figure S3 in Supporting Information S1. The Tilcara Range Frontal Fault is marked in red. Models (b) 6b, (c) 6g, and (d) 6h are shown as the expected t-T-path and 95% confidence interval of the hot and cold sample. Average cooling rates with standard deviation are shown for the most recent exhumation phase. All models show the predicted and observed single-aliquot ages and the LL to the right.

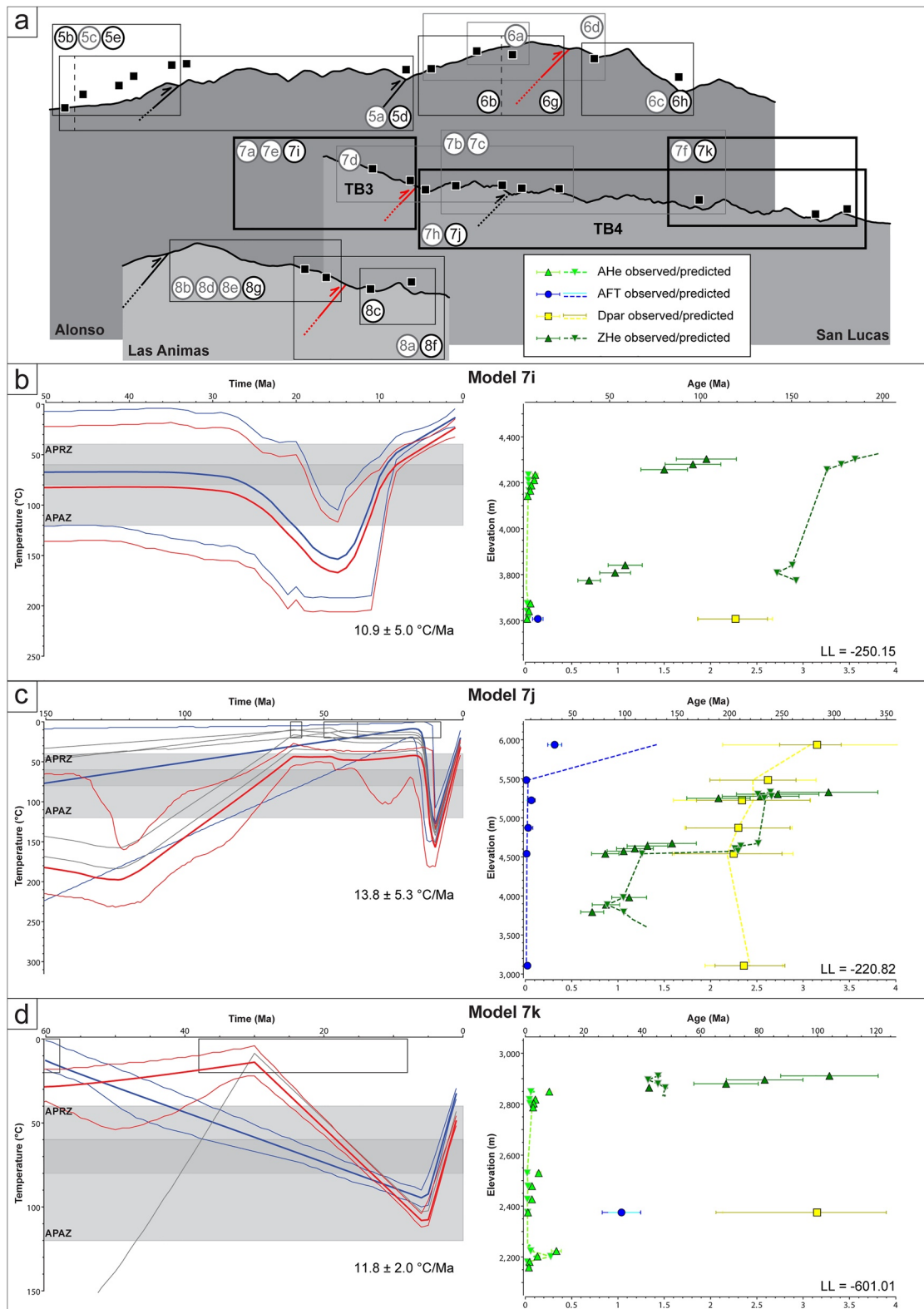


Figure 7. Modeling results for the windward side of the Alonso section. (a) Shows the subset of samples used for individual models (see also Table 3) and its location on the section. Models marked in gray are shown in Figure S3 in Supporting Information S1. The Tilcara Range Frontal Fault is marked in red. Models (b) 7i, (c) 7j and (d) 7k are shown as the expected t-T-path and 95% confidence interval of the hot and cold sample. Average cooling rates with standard deviation are shown for the most recent exhumation phase. All models show the predicted and observed single-aliquot ages and the LL to the right.

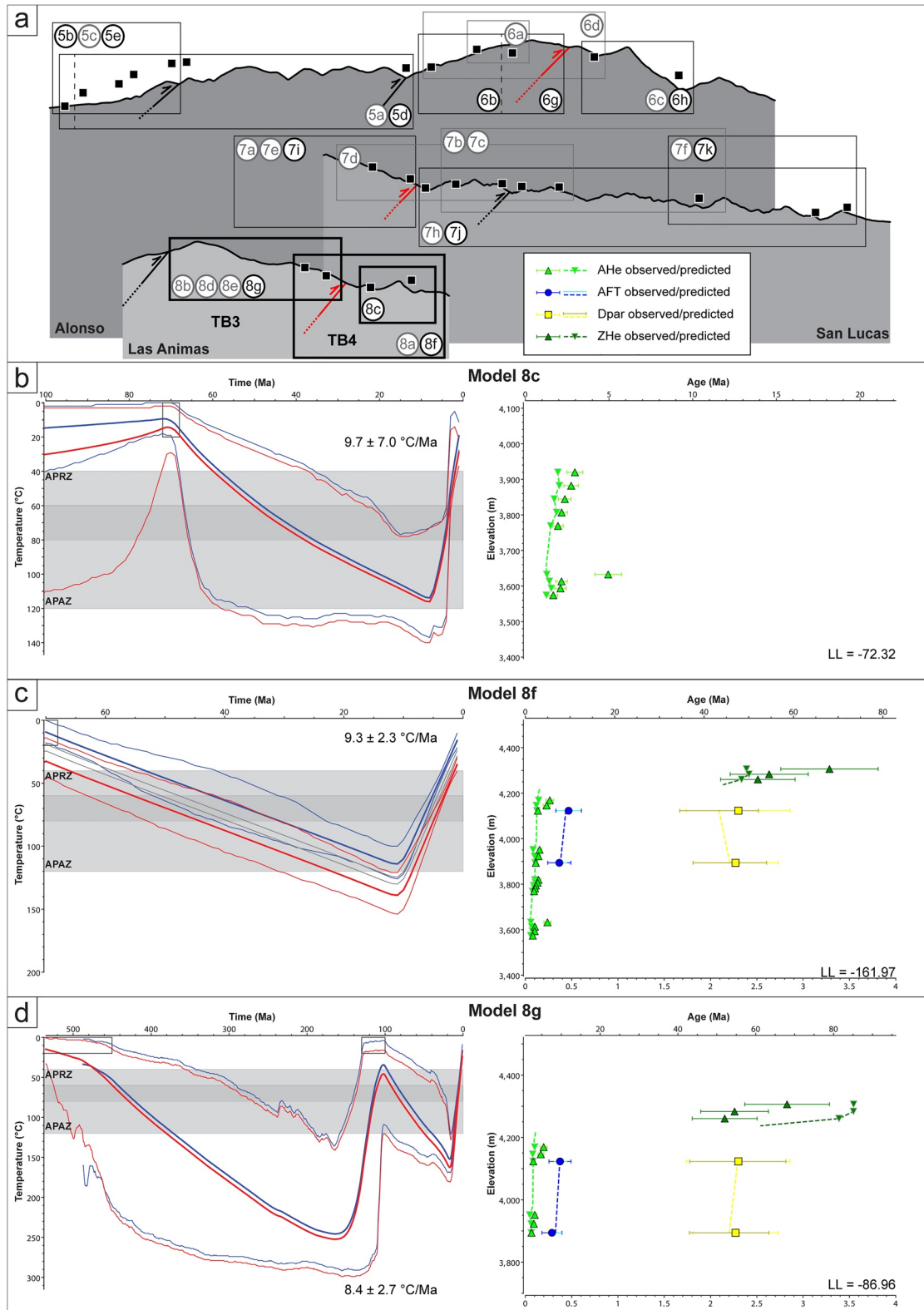


Figure 8. Modeling results for the windward side of the Alonso section. (a) Shows the subset of samples used for individual models (see also Table 3) and its location on the section. Models marked in gray are shown in Figure S3 in Supporting Information S1. The Tilcara Range Frontal Fault is marked in red. Models (b) 8c, (c) 8f, and (d) 8g are shown as the expected t-T-path and 95% confidence interval of the hot and cold sample. Average cooling rates with standard deviation are shown for the most recent exhumation phase. All models show the predicted and observed single-aliquot ages and the LL to the right.

upper Cambrian-lower Ordovician basement to the surface. Although it is clear that the samples were again buried below the APAZ until 60–47 Ma, the timing of Andean exhumation is poorly constrained. Some iterations show an onset of exhumation between 62 and 47 Ma, but a large number of iterations suggest the final pulse of exhumation may have started between 26 and 15 Ma. The latter seems to be more in agreement with the AHe and AFT models.

Miocene-Pliocene exhumation is constrained by AHe, AFT and multi-method models. AHe age-elevation models were run separately for TB3 and TB4 to compare the timing of deformation on both sides of the Tilcara Range Frontal Fault. The TB3 model (model 6b, Figure 6b) shows exhumation starting between 21 and 11 Ma with a slightly decreasing rate of exhumation at approximately 6 Ma. The TB4 model suggests an onset of rapid exhumation between 16 and 15 Ma, within the same interval seen in model 6b (model 6c, Figure S3 in Supporting Information S1), but no decrease of the exhumation rate. We also ran a model across the Tilcara Range Frontal Fault (model 6d, Figure S3 in Supporting Information S1), which proposes an onset of exhumation between 18 and 12 Ma, in between the TB3 and TB4 model. In all cases, the majority of the predicted AHe ages is older than the corresponding observed ages.

We ran separate single-sample AFT models for TB3 and TB4 (model 6e and 6f, respectively). The model for TB3 (model 6e, Figure S3 in Supporting Information S1) suggests an onset of exhumation between 17 and 14 Ma, whereas the model for TB4 (model 6f, Figure S3 in Supporting Information S1) shows continuous exhumation starting between 22 and 17 Ma. The predicted versus observed fit is better for model 6f. The AFT models do not add any significant constraint on the timing of exhumation.

TB3 and TB4 were modeled separately in multi-method, multi-sample models. The TB3 model uses two AHe, one AFT and two ZHe ages in age-elevation space, based on the AHe and ZHe single-method models (model 6g, Figure 6c). It suggests a first pulse of rapid exhumation for the hot sample starting in the Early Cretaceous (133–123 Ma). This is within the exhumation timeframe given by model 7a. From 118 Ma, the samples were buried well below the APAZ (>160°C). Andean exhumation started between 14 and 8 Ma, slowing down between 8 and 7 Ma, coinciding with model 6b. The TB4 model uses two AHe ages in age-elevation space and one AFT age for better constraint (model 6h, Figure 6d). It proposes burial >100°C after deposition of the Santa Bárbara Subgroup at approximately 62 Ma. The onset of continuous exhumation occurred between 18 and 16 Ma, slightly earlier than in AHe model 6c. Again, predicted AHe cooling ages are slightly older than observed ages, but the model fit for AFT and ZHe data is good. Similar to the single-sample AFT models, the onset of exhumation occurred earlier in TB4 than in TB3.

4.3.3. San Lucas Transect

Early pre-Salta Group exhumation was inferred from ZHe models that were run in both age-stratigraphy and age-elevation space. Based on the assumption that block-internal folding and rotation happened after the samples cooled through the ZPRZ, age-stratigraphy trends are theoretically more accurate. However, the effect of the deformation on inter-sample relationships and thermal gradients for the ZHe samples might be too small to notice. The TB3 age-stratigraphy model (model 7a, Figure S3 in Supporting Information S1), although better than the age-elevation model, does not provide good constraints on pre-Salta Group exhumation. Furthermore, predicted ZHe ages are much older than the observed ages. For TB4, the age-elevation (model 7b, Figure S3 in Supporting Information S1) and age-stratigraphy model (model 7c, Figure S3 in Supporting Information S1) yield very similar results with a well-constrained onset of exhumation between 136 and 121 Ma (138 and 112 Ma for model 7c). For this model, ZHe ages show a better observed versus predicted fit. Using a third, Paleogene sample for the TB4 models does not increase the model fit. Unfortunately, none of the models provide good constraints on the timing of Miocene exhumation.

To constrain the Andean exhumation, we ran a multi-sample AHe model (model 7d, Figure S3 in Supporting Information S1) that crosses the Tilcara Range Frontal Fault because of the age-elevation relationship for AHe samples in TB3 and TB4. The model suggests burial at <44 Ma, based on the Santa Bárbara Subgroup depositional age. Miocene exhumation started between 14 and 11 Ma and slowed down after 9 Ma, which is similar to model 5c but earlier than model 6b and 6g. A separate model for TB3 (model 7e, Figure S3 in Supporting Information S1) yields a similar timing of exhumation, starting between 11 and 10 Ma and slowing down between 9 and 8 Ma. In contrast, the easternmost part of TB4 (samples LU9–LU12, model 7f) shows a badly-constrained phase of burial between 30 and 5 Ma below the APRZ and an onset of exhumation between 5 and 4 Ma, much later than models 7d and 7e.

Similar to model 7e, a single-sample AFT model from TB3 (model 7g, Figure S3 in Supporting Information S1) shows an onset of exhumation between 22 and 16 Ma. A multi-sample age-stratigraphy AFT model for TB4, which assumes that most of the block-internal deformation happened after cooling through the APAZ (model 7h, Figure S3 in Supporting Information S1), suggests burial of the cold sample from approximately 27 Ma, followed by rapid exhumation that started between 10 and 8 Ma. This shows that in the San Lucas transect the onset of exhumation in TB4 occurred later than in TB3. Although the model predicts ages that are too old for the upper three samples, it obtains a good Dpar fit throughout the sample column.

We also modeled TB3 and TB4 separately for multi-method models. The age-elevation model for TB3 (model 7i, Figure 7b), using two AHe, one AFT and two ZHe ages with an age-elevation relationship, shows burial below the APAZ from approximately 45 Ma. Exhumation started between 15 and 13 Ma, and slowed down <8 Ma. Similar to the ZHe models, predicted ZHe ages are too old compared to the observed ages, which might be connected to a too-shallow modeled Cenozoic burial of the samples. Although we also ran an age-stratigraphy model with one AFT and two ZHe ages, we prefer the age-elevation model (7i) because of the larger number of constraints placed by the sampling and the resulting constraints on the Miocene exhumation. The use of AFT and ZHe ages in an age-elevation model should not result in major errors, because TB3 is not folded internally and inter-sample relationships are preserved. For TB4 we used age-stratigraphy space, because the AFT samples do not adhere to an age-elevation trend. The model (model 7j, Figure 7c) yields an onset of exhumation at 10 Ma. Even though the uppermost AFT sample shows a predicted age that is too old, the other AFT samples, Dpar values and ZHe ages show a good fit. An age-elevation model of the far eastern part of TB4 (model 7k, Figure 7d) yields an onset of exhumation for the hot sample <6 Ma, roughly coinciding with model 7f. ZHe predicted ages are again too old in this model, for similar reasons as described above.

4.3.4. Las Animas Transect

Although pre-Cretaceous exhumation cannot be constrained well by ZHe models of the Las Animas transect, single- and multi-sample models are able to constrain Miocene exhumation. We ran one AHe model crossing the Tilcara Range Frontal Fault (model 8a, Figure S3 in Supporting Information S1) that suggests exhumation starting before 9 Ma, but the model does not give any hard constraints for the minimum age of onset. The separate age-elevation model for TB3 (model 8b, Figure S3 in Supporting Information S1) yields exhumation beginning between 11 and 10 Ma. The TB4-specific model (model 8c, Figure 8b) shows burial <70 Ma, constrained by the depositional age of the Santa Bárbara Subgroup, and exhumation starting around 15 Ma at the earliest, increasing slightly at approximately 4 Ma. The separate models for TB3 and TB4 both constrain the onset of exhumation better than the combined model and are not affected by fault motion. Furthermore, predicted AHe cooling ages match the observed ages quite well.

Multi-sample age-elevation and age-stratigraphy AFT models for TB3 (model 8d and 8e, Figure S3 in Supporting Information S1) both show similar t-T-paths with an early-middle Miocene onset of exhumation (17-12 Ma and 19-13 Ma, respectively). Unfortunately, both AFT samples in TB4 did not pass the chi-square test and were thus not considered for modeling.

We ran a multi-sample age-elevation model across the Tilcara Range Frontal Fault (model 8f, Figure 8c), which yielded an onset of rapid exhumation at 11 Ma, corresponding to the AHe model for TB3. An age-elevation model for TB3 (model 8g, Figure 8d) shows Late Jurassic-Early Cretaceous exhumation (165-102 Ma), burial at <102 Ma below the APAZ and rapid exhumation beginning between 18 and 16 Ma, coinciding with the earliest timeframe given by the AFT model 8d. Although we ran an age-stratigraphy model, which excluded AHe ages, the Tertiary history of that model was badly constrained whereas the Miocene history was very similar to model 8g. Thus, the age-elevation and age-stratigraphy model show great similarities, indicating that internal deformation after cooling through the ZPRZ and APAZ did not affect the modeling interval for Miocene exhumation.

4.3.5. Summary of Modeling Results

The timing of pre-Salta Group exhumation is well-constrained for both the leeward and windward side of the Tilcara Range. ZHe models from the western Alonso transect show an early phase of exhumation from the Carboniferous to the Early Cretaceous (335-140 Ma), which is confirmed by the multi-method model. However, north of the Alonso transect the Salta Group rests unconformably on top of upper Cambrian-lower Ordovician

(Santa Victoria Group) basement, indicating that the samples may have been close to the surface as late as the Cretaceous (115 ± 15 Ma). The latter is also suggested by ZHe and multi-method models from the windward side, which consistently show a Late Jurassic to Early Cretaceous phase of exhumation (between 150 and 110 Ma), with most of the models showing an onset of exhumation between 140 and 115 Ma.

Cooling related to Andean exhumation began earlier in TB1 and TB2, compared to TB3 and TB4 (Alonso transect), and the cooling rate also shows an earlier decrease in the westernmost tectonic blocks. Furthermore, cooling rates for the most recent Andean exhumation phase are notably lower for the leeward side of the Tilcara Range than for the windward side. Models from the leeward side of the Tilcara Range show an onset of exhumation in the late Oligocene-middle Miocene (26-16 Ma) and two models show a decrease of exhumation rates after 13 Ma. In contrast, the windward side of the Alonso transect shows an onset of exhumation between 21 and 11 Ma for TB3 and 22-15 Ma for TB4, with a decrease in exhumation rate for TB3 around 7 Ma. Models from the San Lucas transect also show a decreasing rate around 7 Ma for TB3. Models from the Alonso, San Lucas and Las Animas transects all show a similar onset of cooling for TB3 (21-11 Ma, 22-10 Ma and 18-11 Ma, respectively). Although for the Alonso and Las Animas transect the onset of exhumation for TB3 and TB4 are roughly contemporaneous, models from the San Lucas transect show a younger onset between 10 and 8 Ma. The San Lucas transect models are theoretically more reliable, because the larger number of samples within this transect encompass a broader swath of stratigraphy and structure. Models for the far eastern part of TB4 (San Lucas transect) show an onset of exhumation between 6 and 4 Ma, younger than the decrease in exhumation rate in TB3 at approximately 7 Ma. This suggests that propagation of fault-related exhumation across the Tilcara Range Frontal Fault occurred in the latest Miocene-earliest Pliocene.

5. Discussion

5.1. Pre-Andean Exhumation

Although the apatite low-temperature thermochronology is only able to show exhumation related to the Andean orogeny, ZHe samples have not received a sufficiently large overprint to erase earlier exhumation events. The majority of ZHe samples from TB1–TB4 record an early period of exhumation within the lower Cretaceous (140-115 Ma), showing an earlier onset than rift shoulder exhumation in the Brealito basin (130-80 Ma, Deeken et al., 2006), the Sierra de Quilmes (105-76 Ma, Carrapa et al., 2014) or at the Cumbres Calchaqu es (Sobel & Strecker, 2003) to the south. Stratigraphic relations of basal Salta Group units overlying basement directly show that Cambrian-Ordovician strata were at the surface during deposition of syn-rift strata. Farther north, the Salta Group overlies Jurassic, Carboniferous and Silurian-Devonian basement (e.g., Siks & Horton, 2011). Whereas the absence of Jurassic and Carboniferous strata in the Tilcara Range is related to the southern boundary of the Tarija basin, which was located along the Michicola arch north of the study area (Starck, 1995), the absence of Silurian-Devonian strata within the Tilcara Range and the San Lucas block shows a marked pre-rift exhumation gradient from north to south (Kley et al., 2005; Starck, 1995). Although the depositional age of the Salta Group was used as a constraint in many models, thus fixing the upper limit of pre-Cretaceous exhumation, several models show an upper limit of cooling in the Cretaceous, regardless of further post-depositional constraints, strongly suggesting a pre-rift exhumation of the Tilcara Range, which we link to normal movement along NW-SE striking faults, associated with Salta rift extension (see also Kley et al., 2005). These faults segment the basement uplifts of the Tilcara Range lithologically but do not offset NNE-SSW striking reverse faults, indicating that these particular pre-existing faults might not have been activated during the most recent phase of the Andean orogeny. In contrast, there is evidence of major inverted normal faults directly north of the study area, within the Cianzo basin (Kley et al., 2005; Siks & Horton, 2011; Starck, 2011).

5.2. Andean Uplift of the Tilcara Range

The Tilcara Range and the San Lucas block were buried by up to 4.5 km of Neogene foreland strata (Siks & Horton, 2011), sourced from the Andean orogenic wedge to the west (DeCelles et al., 2011). However, this burial was not deep enough to reset the zircon helium system; therefore, ZHe data from the Precambrian-Ordovician basement units are unable to document Andean exhumation. Fortunately, low-temperature apatite thermochronology is able to constrain the Miocene-Pliocene history of the Tilcara Range and the San Lucas block. Thermal modeling shows that exhumation of the leeward TB1-TB3 related to the propagation of the Andean wedge started

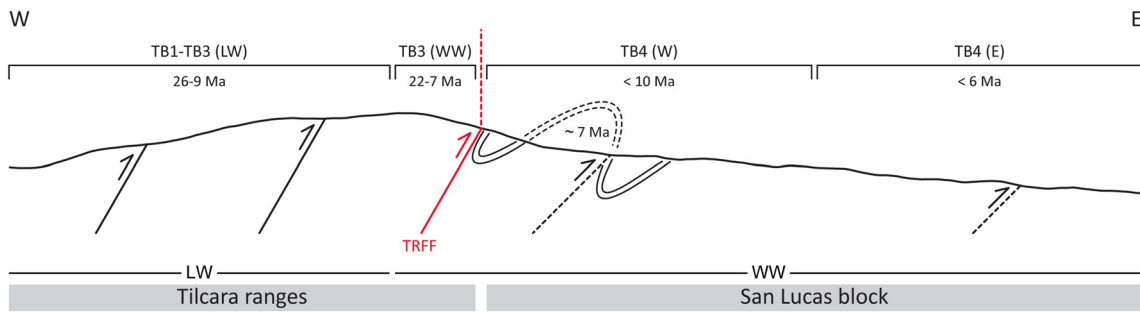


Figure 9. Schematic section showing the timeframe of rapid exhumation for different parts of the Tilcara Range and San Lucas block, inferred from thermal models. Tectonic blocks TB1-TB4, leeward (LW) and windward (WW) side of the Tilcara Range are marked. Detachment(s) in the subsurface (see discussion) are not shown due to scaling issues.

in the late Oligocene-early Miocene (26-16 Ma; Figure 9). Multi-method models also provide a tentative upper constraint for rapid exhumation of TB1, presumably driven by fault activity, between 13 and 12 Ma. AHe cooling ages are not able to constrain the earliest phase of the exhumation, but record a decrease of the exhumation rate <9 Ma, in the late Miocene. Although the latter is in agreement with data from Reynolds et al. (2000), constraining pronounced deformation within the Tilcara Range to 10-4 Ma, reconstructions of Henríquez et al. (2022) suggest shortening and exhumation within the Tilcara Range <6.5 Ma. We propose an earlier onset of exhumation based on thermal modeling. Results from other studies that propose a propagation of deformation from the Puna to the Eastern Cordillera in the late Eocene or early Oligocene (Coutand et al., 2001; Elger et al., 2005; Hongn et al., 2007), also indicate that an early Miocene onset of exhumation at the eastern border of the Eastern Cordillera is plausible.

At the windward side of the Tilcara Range, a general decrease of AHe cooling ages from west to east coincides with lower elevation toward the east and the transition from a high orographic barrier to the Andean foreland. AHe cooling ages in all transects show age-elevation relationships that persist over the Tilcara Range Frontal Fault and NNE-SSW striking intrablock faults. Thermal models for TB3 along all transects indicate a coeval onset of exhumation along-strike. In general, the models suggest that the onset of exhumation for the windward side of the Tilcara Range occurs at a slightly later stage than for the leeward side (leeward: 26-16 Ma, windward: 22-10 Ma). This is in agreement with a systematic younging of cooling ages toward the east (Reiners et al., 2015), as well as an overall eastward propagation of deformation and uplift within the Puna and Eastern Cordillera (Carrapa et al., 2011; Deeken et al., 2006; Gubbels et al., 1993; Henríquez et al., 2022). Furthermore, many models show a decrease of exhumation at ~ 7 Ma, which might serve as an upper constraint for fault-related exhumation of TB3 (Figure 9). Although this disagrees with data from the central part of the Eastern Cordillera, showing that deformation within the Eastern Cordillera ceased at 9-10 Ma (Allmendinger & Zapata, 2000; Gubbels et al., 1993), other studies (Henríquez et al., 2022; Pingel et al., 2013; Reynolds et al., 2000, 2001; Siks & Horton, 2011) suggest that the easternmost border of the Eastern Cordillera was active also in the late Miocene. Rahl et al. (2018) attribute provenance changes in Neogene foreland basin sediments at 23°S to growing topography at the eastern border of the Eastern Cordillera. Similar to the results of Siks and Horton (2011) from the Cianzo basin, they find evidence for blocking of far western sediment sources through the uplift of mountain ranges bounding the Eastern Cordillera by the late Miocene, between 12 and 7 Ma. This is consistent with increasing sedimentation rates in the foreland strata by 9 Ma, because of orographic barrier uplift and increased localization of erosion at the orogenic front (Echavarría et al., 2003). Concurrently, average cooling rates for models at the leeward side of the Tilcara Range are notably lower than cooling rates for the windward side (6.0-6.6°C/Ma leeward vs. 7.2-15.9°C/Ma windward), also indicating more effective erosion at the wet side of the range and the establishment of an orographic barrier during the most recent phase of Andean exhumation in the Miocene-Pliocene. Although denudation rates determined from cosmogenic nuclides (^{10}Be from fluvial sands; Pingel et al., 2019) show a strong variation from 3 Ma, the thermal models show that the uplift of the Tilcara Range must have affected the erosional gradient pre-3 Ma.

5.3. Exhumation Along the Tilcara Range Frontal Fault

The uplift and exhumation of TB1-TB3 was presumably driven by fault activity along the Tilcara Range Frontal Fault, which shows a major change in the structural elevation of the Tilcara Range and San Lucas block. Evidence of fault activity comes from a structural offset of approximately 400 m between the Pirgua Subgroup in TB3 and TB4, east of Alonso. Furthermore, ZHe cooling ages that are younger than the Salta rift-related exhumation phase show a consistent and pronounced offset across the Tilcara Range Frontal Fault in all transects with younger ages in the hanging wall. They indicate fault movement after ~ 50 Ma, coinciding with the stratigraphic and structural lower constraints, given by the youngest stratigraphic unit in its footwall. AFT ages record only a slight offset across the fault and we therefore propose that these ages document the final stages of fault-related exhumation along the Tilcara Range Frontal Fault. This is supported by the continuous AHe age-elevation trend across the Tilcara Range Frontal Fault, proving that fault activity mostly ceased before cooling through the APRZ at ≥ 7 Ma. We thus propose that the upper limit of fault activity along the Tilcara Range Frontal Fault coincides with the decrease in exhumation rate at approximately 7 Ma, and might also mark the propagation of fault activity to the east. Late Miocene-early Pliocene AFT cooling ages from the northern continuation of the Tilcara Range suggest that fault-related exhumation might continue < 7 Ma in parts of the range (Henríquez et al., 2022), although inherited Cretaceous normal faults could be responsible for a segmentation between the Tilcara Range and its northern counterpart. Furthermore, continued exhumation of upper thrust sheets might also be related to an inferred step-down of the basal décollement in the most recent (6.5–0 Ma) time step of Henríquez et al. (2022; Figure 12). In any case, the propagation of exhumation in Argentina from the Eastern Cordillera to its foreland at 23.5°S occurred at a later stage than in Bolivia, where propagation from the Eastern Cordillera into the Interandean Zone happened after 30–25 Ma (Anderson et al., 2018; Ege et al., 2007; McQuarrie et al., 2008; Müller et al., 2002) and propagation from the Interandean Zone into the Subandean Zone occurred between ~ 11 and 8 Ma (Anderson et al., 2018).

5.4. Uplift of the San Lucas Block

Thermal models from the San Lucas block imply an onset of exhumation between 10 and 8 Ma, slightly earlier than the proposed upper limit of fault activity along the Tilcara Range Frontal Fault. However, interpretation of thermal models from the Alonso and Las Animas transects suggests that TB4 started exhuming earlier than TB3, indicating an out-of-sequence propagation of exhumation. The idea of in-sequence eastward propagation of the Andean thrust belt has recently been challenged (Del Papa et al., 2013; Montero-López et al., 2018; Payrola et al., 2020). Instead, it was proposed that deformation has been spatially widespread and disparate in a broken-foreland style (Del Papa et al., 2013; Montero-López et al., 2018). Pearson et al. (2013) suggest that, even though the Andean thrust belt overall propagated toward the east, every eastward pulse prompted a local westward migration of deformation. Out-of-sequence pulses have also been proposed in a very recent study by Henríquez et al. (2022). Our data also suggests that local out-of-sequence uplift of tectonic blocks is possible.

The continuous AHe age-elevation trend within TB4 indicates that internal faulting and folding has transpired before cooling of the samples through the APRZ at ≥ 7 Ma. The timing of deformation within the San Lucas block and final activity along the Tilcara Range Frontal Fault suggests that the competent Tilcara Range acted as a backstop, not dissimilar to the situation at the Eastern Cordillera and Inter-/Subandean Zone, close to the Bolivian border. In contrast, AFT and ZHe ages exhibit approximate age-stratigraphy relationships for TB4, indicating a timing of block-internal deformation during or after cooling through the APAZ. Since the youngest AFT cooling ages in TB4 are approximately 6–7 Ma, deformation within the westernmost San Lucas block occurred before the onset of rapid exhumation in the easternmost part of TB4, suggesting that deformation was still active in the west. Therefore, faulting and folding could have been coeval with the younger most cooling through the APAZ.

Pleistocene AHe cooling ages within the easternmost part of the area show that TB4 was exhumed until very recently. Thermal models show an onset of cooling around 6–4 Ma, coinciding with a decrease of the exhumation rate in TB3, the upper limit of uplift for the Tilcara Range proposed by Reynolds et al. (2000) and recent AFT results from Henríquez et al. (2022). It is again evident that, along-strike to the north, exhumation occurred earlier than in corresponding morphotectonic provinces to the south. For example, the Bolivian Subandean Zone started exhuming < 12 Ma (Anderson et al., 2018; Uba et al., 2007; Uba et al., 2009) and the far eastern part of the Bolivian Subandean Zone shows late Miocene-Pliocene AHe ages (Anderson et al., 2018) that are similar to

the San Lucas block ages. Similarly, exhumation in the Puna at 23–24°S and in the Bolivian Eastern Cordillera at 21°S was coeval (Anderson et al., 2017; Anderson et al., 2018; Elger et al., 2005; Henríquez et al., 2020; Henríquez et al., 2022; Müller et al., 2002). More recent Pliocene-Pleistocene exhumation of TB4 may be explained by uplift along underlying, potentially blind thrust faults that nucleate from a basal detachment. On the other hand, González and Tchilinguirian (2003) show inferred reverse or thrust faults cropping out east of the Calilegua National Park (Figure 1a). Along-strike to the north, these outcrops appear to coincide with the easternmost border of the Interandean Zone in Bolivia (Kley, 1996). Furthermore, close to the Calilegua National Park, a 2009 earthquake recorded thrust faulting in an ESE (104°) direction at the shallow depth of 5 km (Heidbach et al., 2016, 2018), suggesting that the thrusts driving exhumation of TB4 continue to be active.

5.5. Structural Implications

East-vergent, high-angle reverse faults within Precambrian to Ordovician strata, segmenting the basement blocks of the Tilcara Range, are associated with rotation of the blocks along a N-S oriented, (sub)horizontal axis, causing a tilting of the strata toward the west. The high-angle character of the faults suggests that these might be reactivated and possibly related to pre-existing structures from the Ocluyic phase, which also affect the present-day structure of the Eastern Cordillera (Alonso et al., 2012; Hongn et al., 2010; Salfity & Marquillas, 1994; Starck et al., 1992). For example, in the westernmost part of the study area, retrodeformation of Andean east-vergent thrusting reveals Paleozoic east-vergent shortening in the Precambrian-Ordovician basement (Barrabino et al., 2015). Regional evidence of Paleozoic inherited structures is found for example, west of the Quebrada de Humahuaca (Alonso et al., 2012; Mon et al., 1993; Seggiaro & Gallardo, 2002) and east of Salta (Seggiaro et al., 2014). In general, Paleozoic folding shows a higher amplitude and shorter wavelength than Andean deformation (see also Barrabino et al., 2015), which is highlighted by the angular unconformity between the Salta Group and previously folded Santa Victoria Group strata. Although many of the aforementioned Paleozoic structures relate to a convergent setting, an influence of early to middle Ordovician normal faulting has also been debated (see Figure 2c in this study and discussion in Seggiaro et al., 2017).

East of the Tilcara Range Frontal Fault, the San Lucas block shows close, in part overturned folds within the Cretaceous to Paleogene strata, forming east-vergent footwall synclines (Figure 2c). The amount of shortening decreases toward the east, as is evident from the increasing open fold geometry observed from Huairahuasi to San Lucas (see also Henríquez et al., 2022). Coinciding with the structural change from high-angle uplifts of deeper basement rocks within the Tilcara Range to a more fold-dominated style and lower-angle reverse faults within the San Lucas block is a marked exhumation gradient: the Salta Group overlies the deformed Santa Victoria Group sedimentary basement directly both west and east of the Tilcara Range, but the range itself is mainly built of the Precambrian-Cambrian Puncoviscana Fm and Mesón Group (see also González & Tchilinguirian, 2003; Salfity & Marquillas, 1994) with locally constricted, small outcrops of the Salta Group. The absence of syn-rift and foreland basin deposits within the Tilcara Range indicates that major exhumation has taken place after the establishment of an orographic barrier in the Andean phase. However, the sharp contacts between the Puncoviscana Formation and the Santa Victoria Group along NE-SW striking faults, which coincidentally form the local half-grabens in which the syn-rift deposits were shed, also suggest a high amount of pre-Cretaceous exhumation.

The structural elevation and lithological contrast between the Tilcara Range and the San Lucas block show similarities to the transition between the Eastern Cordillera and Interandean Zone in southern Bolivia (Kley, 1996), where the thick-skinned Eastern Cordillera fold-and-thrust belt exhibits high-angle, east-vergent basement faults that ultimately root in a detachment at 8–10 km depth (Kley, 1996). This shallow detachment level continues to the east, underneath the Interandean Zone (Allmendinger & Zapata, 2000; Kley, 1996). A frontal, high-angle reverse fault separates the Eastern Cordillera from the Interandean Zone, which at the surface shows characteristics of a thin-skinned fold-and-thrust belt but rides on top of a basement thrust sheet (Kley, 1996; McQuarrie, 2002). In NW Argentina, the detachment below the Puna and part of the Eastern Cordillera is located at a similar depth of ~10 km, ramping upwards to ultimately form the northern continuation of the Tilcara Range Frontal Fault at the surface (Henríquez et al., 2022). Based on all of the aforementioned, the Tilcara Range Frontal Fault and its apparent northern continuation, the Cianzo thrust (reverse fault) (Siks & Horton, 2011), may very well be the along-strike equivalent of the frontal reverse fault of the Sama-Yunchará anticlinorium (Figure 1a, SYA), forming the boundary of the Eastern Cordillera in Bolivia. However, toward the south, the Interandean Zone located east

of the SYA increasingly disappears and structures east of the Tilcara Range are generally considered to belong to the Eastern Cordillera (see e.g., [Henríguez et al., 2022](#)).

Although thermochronological cooling ages from the San Lucas block and its northern continuation ([Henríguez et al., 2022](#)) are similar to the easternmost Subandean Zone of Bolivia, we cannot consider the San Lucas block to be the direct equivalent of the Subandean Zone from a structural point of view. The boundary between the Eastern Cordillera and Interandean Zone in Bolivia is marked by the transition at the basement-cover interface from competent Cambrian quartzite into incompetent Silurian shales ([Anderson et al., 2018](#); [Kley, 1996](#)). Consequently, the main detachment level within the thin-skinned Subandean Zone ([Dunn et al., 1995](#); [Echavarría et al., 2003](#); [Gubbels et al., 1993](#); [Kley, 1996](#)) is located within these Silurian shales, dipping gently (2–3°) toward the west (see e.g., [Anderson et al., 2017](#); [Echavarría et al., 2003](#); [McQuarrie, 2002](#)). The termination of thin-skinned deformation at 23°S, coinciding with the margin of the Lomas de Olmedo sub-basin, is attributed to the increased erosion of the Silurian-Devonian section toward the south ([Starck, 1995](#)) and the removal of these incompetent, potential detachment horizons ([Kley & Monaldi, 2002](#)), which are absent within the San Lucas block ([Figure 2](#)). Furthermore, although it was proposed that the Subandean detachment is located at depths of >24 km beneath the Santa Barbara System ([Allmendinger & Zapata, 2000](#)), the slip recorded by earthquake focal mechanisms east of the study area ([Figure 1a](#)) cannot be related to this detachment, because it occurred at too shallow depth ([Heidbach et al., 2016, 2018](#)). Solving this problem is beyond the scope of this work, but previous studies have presented various solutions for the crustal structure of the Central Andes at this longitude. In one model, [Cahill et al. \(1992\)](#) propose an upward ramping of the detachment below the Santa Barbara System, based on seismicity patterns and focal mechanism solutions. In a more recent study, [McFarland et al. \(2017\)](#) infer a basal thrust belt detachment at approximately 15 km depth beneath the Eastern Cordillera, with a freely slipping portion to the west, showing no microseismicity, and a fully locked portion below the San Lucas block, showing microseismicity (data from [Cahill et al., 1992](#)). A very recent study by [Henríguez et al. \(2022\)](#) proposes a detachment at the base of the Ordovician strata, at ~10 km depth beneath the Puna, which reaches the surface as the along-strike continuation of the Tilcara Range Frontal Fault. They propose a second detachment beneath the northern continuation of the San Lucas block, located at ~18 km depth, but ramping upwards to shallower levels beneath the eastern part of the study area.

South of 23.5°S, the Subandean Zone is replaced by the thick-skinned Santa Barbara System, which is characterized by basement uplifts along pre-existing faults and sparse low-angle Tertiary faults ([Kley & Monaldi, 2002](#)). Based on the thickness of the Cambrian-Ordovician strata and the inferred high-angle (>30°) geometry of block-internal faults, deformation of the San Lucas block also shows involvement of Precambrian-Cambrian, weakly metamorphosed basement rocks. However, footwall synclines within Tertiary strata, which are classically related to thrusting ([McNaught & Mitra, 1993](#)), and short-wavelength folds in general are more widespread. Furthermore, the main detachment level within a thick-skinned fold-and-thrust belt is generally at greater depth than recorded by the 2009 earthquake east of Calilegua ([Piffner, 2017](#)). Simple geometric extrapolation of a 5° west-dipping detachment located at 5 km depth below the Calilegua National Park toward the west shows that this detachment would be located at approximately 12 km depth below the Tilcara Range and the San Lucas block, similar to the depth of the Eastern Cordillera/Interandean Zone detachment in the Bolivian fold-and-thrust belt ([Kley, 1996](#)) and the detachment beneath the Eastern Cordillera and Puna in NW Argentina ([Henríguez et al., 2022](#)). Such a shallow detachment is able to invoke thrust faults, relatively low-angle reverse faults and short-wavelength folding at the surface. At the same time, a deeper detachment may be responsible for crustal thickening and propagation of deformation into the Andean foreland, but might also be able to influence exhumation in shallower crustal levels. Hybrid models showing a combination of thick- and thin-skinned deformation have been documented by for example, [Giambiagi et al. \(2008, 2009\)](#) and [Parker and Pearson \(2021\)](#). To study their application to the Tilcara Range and San Lucas block, more detailed structural mapping and modeling, especially of the Santa Victoria Group and its relationship to the overlying Salta Group, is needed.

6. Conclusions

Thermal modeling within a structural context provides quantitative constraints on the deformation and exhumation history of the Tilcara Range and San Lucas block. Placed within a broader reference frame, the low-temperature AHe, AFT, and ZHe data set imposes new constraints on the multi-phase exhumation history of the Eastern Cordillera in NW Argentina ([Figure 9](#)). We extract four key conclusions from our study:

1. Thermal models using ZHe single-grain ages record a cooling event between approximately 140 and 115 Ma, corresponding to pre-Salta Group exhumation of basement highs in the early stages of the Salta Rift. In particular the lower limit is newly constrained by thermal models in this study.
2. Exhumation related to the Andean orogeny began in the latest Oligocene-early Miocene (26–16 Ma) at the westernmost border of the Tilcara Range and propagated toward the east, reaching the eastern part of the range in the early-middle Miocene (22–10 Ma), the western San Lucas block in the late Miocene (10–8 Ma) and the eastern San Lucas block in the early Pliocene (6–4 Ma). Individual thermal models indicate out-of-sequence deformation at a local scale, although at a larger scale, deformation appears to occur in-sequence.
3. The Tilcara Range Frontal Fault forms the structural boundary between the thick-skinned Tilcara Range and the San Lucas block, which is characterized by short-wavelength folds and lower-angle reverse faults. Thermal models indicate that rapid exhumation of the easternmost Tilcara Range began in the early Neogene and ended around 7 Ma. AHe cooling ages show continuous age-elevation relationships across the Tilcara Range Frontal Fault, confirming that major fault-related exhumation ceased in the late Miocene (≥ 7 Ma) and rapid exhumation in the western San Lucas block began coevally.
4. Internal faulting and folding of the San Lucas block predates final fault-related exhumation at the Tilcara Range Frontal Fault and disturbs age-elevation relationships between ZHe and AFT samples. Thermochronologically, the San Lucas block is the equivalent of the Subandean Zone, with cooling ages showing that its western part started exhuming in the late Miocene (10–8 Ma), while its eastern part started exhuming in the late Miocene-early Pliocene (5–4 Ma). Recent earthquake focal mechanisms show that faults east of Valle Grande, which may drive exhumation of the San Lucas block, have been active recently.

Data Availability Statement

Data associated with this paper can be found in the Supporting Information at <https://doi.org/10.5281/zenodo.6358993>.

Acknowledgments

This research was funded by the Deutsche Forschungsgemeinschaft (DFG) International Research Training Group IGK2018 (STRATEGY), grant number STR373/34-1 at the University of Potsdam. We sincerely thank Maria Florencia Wayar Córdoba and Tamara Toledo for support during field campaigns. We also thank Juan Speroni and Sebastian Lamas and his family for logistical assistance and Alejandro Nieva for mineral separations at the Universidad Nacional de Salta. Careful reviews by Laura Giambiagi, Massimiliano Zattin and an anonymous reviewer have substantially improved the manuscript.

References

- Aceñolaza, G. F. (2003). The Cambrian system in northwestern Argentina: Stratigraphical and palaeontological framework. *Geologica Acta*, 1, 23–39. <https://doi.org/10.1344/105.000001590>
- Adams, C. J., Miller, H., Aceñolaza, G. F., Toselli, A. J., & Griffin, W. L. (2011). The Pacific Gondwana margin in the late Neoproterozoic–early Paleozoic: Detrital zircon U–Pb ages from metasediments in northwest Argentina reveal their maximum age, provenance and tectonic setting. *Gondwana Research*, 19(1), 71–83. <https://doi.org/10.1016/j.gr.2010.05.002>
- Allmendinger, R. W., & Zapata, T. R. (2000). The footwall ramp of the Subandean decollement, northernmost Argentina, from extended correlation of seismic reflection data. *Tectonophysics*, 321(1), 37–55. [https://doi.org/10.1016/S0040-1951\(00\)00077-9](https://doi.org/10.1016/S0040-1951(00)00077-9)
- Alonso, J. L., Seggiaro, R. E., Quintana, L., Gallastegui, J., Bulnes, M., Poblet, J., et al. (2012). Deformaciones paleozoicas en la Cordillera Oriental de los Andes a los 23°S (NO de Argentina). 8° Congreso Geológico de España, Actas, (Vol. 13, pp. 1844–1847).
- Anderson, M., Alvarado, P., Zandt, G., & Beck, S. L. (2007). Geometry and brittle deformation of the subducting Nazca Plate, Central Chile and Argentina. *Geophysical Journal International*, 171(1), 419–434. <https://doi.org/10.1111/j.1365-246X.2007.03483.x>
- Anderson, R. B., Long, S. P., Horton, B. K., Calle, A. Z., & Ramirez, V. (2017). Shortening and structural architecture of the Andean fold-thrust belt of southern Bolivia (21°S): Implications for kinematic development and crustal thickening of the central Andes. *Geosphere*, 13(2), 538–558. <https://doi.org/10.1130/GES01433.1>
- Anderson, R. B., Long, S. P., Horton, B. K., Thomson, S. N., Calle, A. Z., & Stockli, D. F. (2018). Orogenic wedge evolution of the central Andes, Bolivia (21°S): Implications for Cordilleran cyclicity. *Tectonics*, 37(10), 3577–3609. <https://doi.org/10.1029/2018TC005132>
- Arriagada, C., Roperch, P., Mpodozis, C., & Cobbold, P. R. (2008). Paleogene building of the Bolivian Orocline: Tectonic restoration of the central Andes in 2-D map view. *Tectonics*, 27(6). <https://doi.org/10.1029/2008TC002269>
- Bahlburg, H., Moya, M. C., Zimmermann, U., Bock, B., & Hervé, F. (2000). Paleozoic plate tectonic evolution of the western Gondwana margin in northern Chile and northwestern Argentina. In H. Miller & F. Hervé (Eds.), *Zeitschrift für Angewandte Geologie, Sonderheft SH1* (pp. 345–353).
- Barbarand, J., Carter, A., Wood, I., & Hurford, A. J. (2003). Compositional and structural control of fission-track annealing in apatite. *Chemical Geology*, 198(1–2), 107–137. [https://doi.org/10.1016/S0009-2541\(02\)00424-2](https://doi.org/10.1016/S0009-2541(02)00424-2)
- Barnes, J. B., Ehlers, T. A., McQuarrie, N., O’Sullivan, P., & Tawackoli, S. (2008). Thermochronometer record of central Andean Plateau growth, Bolivia (19.5°S). *Tectonics*, 27(3). <https://doi.org/10.1029/2007TC002174>
- Barrabino, E., Seggiaro, R. E., Ramos, J. J., Villagrán, C., & Celedón, M. (2015). Análisis estructural del valle de Alfarcito-Punta Corral, Quebrada de Humahuaca, Provincia de Jujuy. 16° Reunión de Tectónica. (pp. 70–71).
- Becker, T. P., Summa, L. L., Ducea, M. N., & Karner, G. D. (2015). Temporal growth of the Puna Plateau and its bearing on the post-Salta Rift system subsidence of the Andean foreland basin at 25°30’S. In P. G. DeCelles, M. N. Ducea, B. Carrapa, & P. A. Kapp (Eds.), *Geodynamics of a cordilleran orogenic system: The central Andes of Argentina and northern Chile*. Geological Society of America. [https://doi.org/10.1130/2015.1212\(20\)](https://doi.org/10.1130/2015.1212(20))
- Boll, A., Gómez Omil, R. J., & Hernández, R. M. (1989). Síntesis Estratigráfica del Grupo Salta: Informe inédito YPF.
- Boll, A., & Hernández, R. M. (1986). Interpretación estructural del área Tres Cruces. *Boletín de Informaciones Petroleras*, 7, 2–14.
- Bookhagen, B., & Strecker, M. R. (2012). Spatiotemporal trends in erosion rates across a pronounced rainfall gradient: Examples from the southern Central Andes. *Earth and Planetary Science Letters*, 327–328, 97–110. <https://doi.org/10.1016/j.epsl.2012.02.005>

- Buatois, L. A., Zeballos, F. J., Albanesi, G. L., Ortega, G., Vaccari, N. E., & Mángano, M. G. (2006). Depositional environments and stratigraphy of the upper Cambrian-lower ordovician Santa rosita formation at the alfarcito area, Cordillera oriental, Argentina: Integration of biostratigraphic data within a sequence stratigraphic framework. *Latin American Journal of Sedimentology and Basin Analysis*, 13, 1–29.
- Cahill, T., Isacks, B. L., Whitman, D., Chatelain, J.-L., Perez, A., & Chiu, J. M. (1992). Seismicity and tectonics in Jujuy province, northwestern Argentina. *Tectonics*, 11(5), 944–959. <https://doi.org/10.1029/92TC00215>
- Carlson, W. D., Donelick, R. A., & Ketcham, R. A. (1999). Variability of apatite fission-track annealing kinetics: I, Experimental results. *American Mineralogist*, 84(9), 1213–1223. <https://doi.org/10.2138/am-1999-0901>
- Carrapa, B., Bywater-Reyes, S., DeCelles, P. G., Mortimer, E., & Gehrels, G. E. (2012). Late eocene-pliocene basin evolution in the eastern Cordillera of northwestern Argentina (25°–26°S): Regional implications for andean orogenic wedge development. *Basin Research*, 24(3), 249–268. <https://doi.org/10.1111/j.1365-2117.2011.00519.x>
- Carrapa, B., & DeCelles, P. G. (2008). Eocene exhumation and basin development in the Puna of northwestern Argentina. *Tectonics*, 27(1). <https://doi.org/10.1029/2007TC002127>
- Carrapa, B., Reyes-Bywater, S., Safipour, R., Sobel, E. R., Schoenbohm, L. M., DeCelles, P. G., et al. (2014). The effect of inherited paleotopography on exhumation of the Central Andes of NW Argentina. *The Geological Society of America Bulletin*, 126(1–2), 66–77. <https://doi.org/10.1130/B30844.1>
- Carrapa, B., Trimble, J. D., & Stockli, D. F. (2011). Patterns and timing of exhumation and deformation in the Eastern Cordillera of NW Argentina revealed by (U-Th)/He thermochronology. *Tectonics*, 30(3). <https://doi.org/10.1029/2010TC002707>
- Carrera, N., Muñoz, J. A., Sàbat, F., Mon, R., & Roca, E. (2006). The role of inversion tectonics in the structure of the Cordillera Oriental (NW Argentinean Andes). *Journal of Structural Geology*, 28(11), 1921–1932. <https://doi.org/10.1016/j.jsg.2006.07.006>
- Copernicus WorldDEM-30 (2021). © DLR e.V. 2010-2014 and © Airbus Defence and Space GmbH 2014-2018.
- Coutand, I., Cobbold, P. R., Urreiztieta, M., Gautier, P., Chauvin, A., Gapais, D., et al. (2001). Style and history of Andean deformation, Puna plateau, northwestern Argentina. *Tectonics*, 20(2), 210–234. <https://doi.org/10.1029/2000TC900031>
- DeCelles, P. G., Carrapa, B., & Gehrels, G. E. (2007). Detrital zircon U-Pb ages provide provenance and chronostratigraphic information from Eocene synorogenic deposits in northwestern Argentina. *Geology*, 35(4), 323. <https://doi.org/10.1130/G23322A.1>
- DeCelles, P. G., Carrapa, B., Horton, B. K., & Gehrels, G. E. (2011). Cenozoic foreland basin system in the central Andes of northwestern Argentina: Implications for Andean geodynamics and modes of deformation. *Tectonics*, 30(6). <https://doi.org/10.1029/2011TC002948>
- DeCelles, P. G., & Horton, B. K. (2003). Early to middle Tertiary foreland basin development and the history of Andean crustal shortening in Bolivia. *The Geological Society of America Bulletin*, 115(1), 58–77. [https://doi.org/10.1130/0016-7606\(2003\)115<0058:ETMTFB>2.0.CO;2](https://doi.org/10.1130/0016-7606(2003)115<0058:ETMTFB>2.0.CO;2)
- Deeken, A., Sobel, E. R., Coutand, I., Haschke, M., Riller, U., & Strecker, M. R. (2006). Development of the southern Eastern Cordillera, NW Argentina, constrained by apatite fission track thermochronology: From early Cretaceous extension to middle Miocene shortening. *Tectonics*, 25(6). <https://doi.org/10.1029/2005tc001894>
- Del Papa, C. E., Hongn, F. D., Powell, J., Payrola, P., Do Campo, M., Strecker, M. R., et al. (2013). Middle Eocene-Oligocene broken-foreland evolution in the Andean Calchaqui Valley, NW Argentina: Insights from stratigraphic, structural and provenance studies. *Basin Research*, 25(5), 574–593. <https://doi.org/10.1111/bre.12018>
- Del Papa, C. E., Kirschbaum, A., Powell, J., Brod, A., Hongn, F. D., & Pimentel, M. M. (2010). Sedimentological, geochemical and paleontological insights applied to continental omission surfaces: A new approach for reconstructing an eocene foreland basin in NW Argentina. *Journal of South American Earth Sciences*, 29(2), 327–345. <https://doi.org/10.1016/j.jsames.2009.06.004>
- Donelick, R. A. (1993). A method of fission track analysis utilizing bulk chemical etching of apatite, Patent no. 5,267,274.
- Donelick, R. A. (2005). Apatite fission-track analysis. *Reviews in Mineralogy and Geochemistry*, 58(1), 49–94. <https://doi.org/10.2138/rmg.2005.58.3>
- Donelick, R. A., Ketcham, R. A., & Carlson, W. D. (1999). Variability of apatite fission-track annealing kinetics: II, Crystallographic orientation effects. *American Mineralogist*, 84(9), 1224–1234. <https://doi.org/10.2138/am-1999-0902>
- Dumitru, T. (1994). FTStage [software].
- Dunn, J. F., Hartshorn, K. G., & Hartshorn, P. W. (1995). Structural styles and hydrocarbon potential of the sub-andean thrust belt of southern Bolivia. In A. J. Tankard, R. S. Soruco, & H. J. Welsink (Eds.), *Petroleum basins of South America*. American Association of Petroleum Geologists. <https://doi.org/10.1306/M62593C27>
- Echavarría, L., Hernández, R. M., Allmendinger, R. W., & Reynolds, J. H. (2003). Subandean thrust and fold belt of northwestern Argentina: Geometry and timing of the Andean evolution. *AAPG Bulletin*, 87(6), 965–985. <https://doi.org/10.1306/01200300196>
- Ege, H., Sobel, E. R., Scheuber, E., & Jacobshagen, V. (2007). Exhumation history of the southern Altiplano plateau (southern Bolivia) constrained by apatite fission track thermochronology. *Tectonics*, 26(1). <https://doi.org/10.1029/2005TC001869>
- Eichelberger, N., McQuarrie, N., Ehlers, T. A., Enkelmann, E., Barnes, J. B., & Lease, R. O. (2013). New constraints on the chronology, magnitude, and distribution of deformation within the central Andean orocline. *Tectonics*, 32(5), 1432–1453. <https://doi.org/10.1002/tect.20073>
- Einhorn, J. C., Gehrels, G. E., Vernon, A., & DeCelles, P. G. (2015). U-Pb zircon geochronology of Neoproterozoic–Paleozoic sandstones and Paleozoic plutonic rocks in the Central Andes (21°S–26°S). In P. G. DeCelles, M. N. Ducea, B. Carrapa, & P. A. Kapp (Eds.), *Geodynamics of a cordilleran orogenic system: The central Andes of Argentina and northern Chile*. Geological Society of America. <https://doi.org/10.1130/2015.1212/06>
- Elger, K., Oncken, O., & Glodny, J. (2005). Plateau-style accumulation of deformation: Southern Altiplano. *Tectonics*, 24(4). <https://doi.org/10.1029/2004TC001675>
- Escayola, M. P., Van Staal, C. R., & Davis, W. J. (2011). The age and tectonic setting of the Puncoviscana Formation in northwestern Argentina: An accretionary complex related to Early Cambrian closure of the Puncoviscana Ocean and accretion of the Arequipa-Antofalla block. *Journal of South American Earth Sciences*, 32(4), 438–459. <https://doi.org/10.1016/j.jsames.2011.04.013>
- Esri. (2021). Esri World Imagery (WGS84). Retrieved from <http://www.arcgis.com/home/item.html?id=898f58f2ee824b3c97bae0698563a4b3>
- Farley, K. A. (2000). Helium diffusion from apatite: General behavior as illustrated by Durango fluorapatite. *Journal of Geophysical Research*, 105(B2), 2903–2914. <https://doi.org/10.1029/1999JB900348>
- Farley, K. A., Wolf, R. A., & Silver, L. T. (1996). The effects of long alpha-stopping distances on (U-Th)/He ages. *Geochimica et Cosmochimica Acta*, 60(21), 4223–4229. [https://doi.org/10.1016/S0016-7037\(96\)00193-7](https://doi.org/10.1016/S0016-7037(96)00193-7)
- Flowers, R. M., Ketcham, R. A., Shuster, D. L., & Farley, K. A. (2009). Apatite (U-Th)/He thermochronometry using a radiation damage accumulation and annealing model. *Geochimica et Cosmochimica Acta*, 73(8), 2347–2365. <https://doi.org/10.1016/j.gca.2009.01.015>
- Galbraith, R. F., & Laslett, G. M. (1993). Statistical models for mixed fission track ages. *Nuclear Tracks and Radiation Measurements*, 21(4), 459–470. [https://doi.org/10.1016/1359-0189\(93\)90185-C](https://doi.org/10.1016/1359-0189(93)90185-C)

- Galetto, A., Georgieva, V., García, V. H., Zattin, M., Sobel, E. R., Glodny, J., et al. (2021). Cretaceous and Eocene rapid cooling phases in the southern Andes (36°–37°S): Insights from low-temperature thermochronology, U-Pb geochronology, and inverse thermal modeling from Domuyo area, Argentina. *Tectonics*, *40*(6). <https://doi.org/10.1029/2020TC006415>
- Gallagher, K. (2021). QTQt. (v5.8.0) [software].
- Gallagher, K., Charvin, K., Nielsen, S., Sambridge, M., & Stephenson, J. (2009). Markov chain Monte Carlo (MCMC) sampling methods to determine optimal models, model resolution and model choice for Earth Science problems. *Marine and Petroleum Geology*, *26*(4), 525–535. <https://doi.org/10.1016/j.marpetgeo.2009.01.003>
- Gans, C. R., Beck, S. L., Zandt, G., Gilbert, H., Alvarado, P., Anderson, M., & Linkimer, L. (2011). Continental and oceanic crustal structure of the pampean flat slab region, western Argentina, using receiver function analysis: New high-resolution results. *Geophysical Journal International*, *186*(1), 45–58. <https://doi.org/10.1111/j.1365-246X.2011.05023.x>
- Giambiagi, L., Bechis, F., García, V., & Clark, A. H. (2008). Temporal and spatial relationships of thick- and thin-skinned deformation: A case study from the Malargüe fold-and-thrust belt, southern Central Andes. *Tectonophysics*, *459*(1–4), 123–139. <https://doi.org/10.1016/j.tecto.2007.11.069>
- Giambiagi, L., Ghiglione, M., Cristallini, E., & Bottesi, G. (2009). Kinematic models of basement/cover interaction: Insights from the Malargüe fold and thrust belt, Mendoza, Argentina. *Journal of Structural Geology*, *31*(12), 1443–1457. <https://doi.org/10.1016/j.jsg.2009.10.006>
- Gleadow, A. (1981). Fission-track dating methods: What are the real alternatives? *Nuclear Tracks*, *5*(1–2), 3–14. [https://doi.org/10.1016/0191-278X\(81\)90021-4](https://doi.org/10.1016/0191-278X(81)90021-4)
- González, M. A., & Tchilinguirian, P. (2003). *Hoja Geológica 2366-IV, San Martín: Ciudad de Libertador general san Martín*. Instituto de Geología y Recursos Minerales (SEGEMAR).
- Google (n.d.). Google Earth Pro Imagery (v7.3.4.8642). *NW Argentina* [Software].
- Green, P. F. (1981). A new look at statistics in fission-track dating. *Nuclear Tracks*, *5*(1–2), 77–86. [https://doi.org/10.1016/0191-278X\(81\)90029-9](https://doi.org/10.1016/0191-278X(81)90029-9)
- Grier, M. E., Salfity, J. A., & Allmendinger, R. W. (1991). Andean reactivation of the Cretaceous Salta rift, northwestern Argentina. *Journal of South American Earth Sciences*, *4*(4), 351–372. [https://doi.org/10.1016/0895-9811\(91\)90007-8](https://doi.org/10.1016/0895-9811(91)90007-8)
- Gubbels, T. L., Isacks, B. L., & Farrar, E. (1993). High-level surfaces, plateau uplift, and foreland development, Bolivian central Andes. *Geology*, *21*(8), 695. [https://doi.org/10.1130/0091-7613\(1993\)021<0695:HLSPUA>2.3.CO;2](https://doi.org/10.1130/0091-7613(1993)021<0695:HLSPUA>2.3.CO;2)
- Guenther, W. R., Reiners, P. W., DeCelles, P. G., & Kendall, J. (2015). Sevier belt exhumation in central Utah constrained from complex zircon (U-Th)/He data sets: Radiation damage and He inheritance effects on partially reset detrital zircons. *The Geological Society of America Bulletin*, *127*(3–4), 323–348. <https://doi.org/10.1130/B31032.1>
- Guenther, W. R., Reiners, P. W., Ketcham, R. A., Nasdala, L., & Giester, G. (2013). Helium diffusion in natural zircon: Radiation damage, anisotropy, and the interpretation of zircon (U-Th)/He thermochronology. *American Journal of Science*, *313*(3), 145–198. <https://doi.org/10.2475/03.2013.01>
- Heidbach, O., Rajabi, M., Cui, X., Fuchs, K., Müller, B., Reinecker, J., et al. (2018). The World Stress Map database release 2016: Crustal stress pattern across scales. *Tectonophysics*, *744*, 484–498. <https://doi.org/10.1016/j.tecto.2018.07.007>
- Heidbach, O., Rajabi, M., Reiter, K., Ziegler, M., & WSM Team. (2016). World Stress Map Database Release 2016, GFZ Data Services. <http://doi.org/10.5880/WSM.2016.001>
- Henríquez, S., DeCelles, P. G., & Carrapa, B. (2019). Cretaceous to middle cenozoic exhumation history of the Cordillera de Domeyko and Salar de Atacama basin, northern Chile. *Tectonics*, *38*(2), 395–416. <https://doi.org/10.1029/2018TC005203>
- Henríquez, S., DeCelles, P. G., Carrapa, B., & Hughes, A. N. (2022). Kinematic evolution of the central Andean retroarc thrust belt in northwestern Argentina and implications for coupling between shortening and crustal thickening. *Geological Society of America Bulletin*. <https://doi.org/10.1130/B36231.1>
- Henríquez, S., DeCelles, P. G., Carrapa, B., Hughes, A. N., Davis, G. H., & Alvarado, P. (2020). Deformation history of the Puna plateau, central Andes of northwestern Argentina. *Journal of Structural Geology*, *140*, 104133. <https://doi.org/10.1016/j.jsg.2020.104133>
- Heredia, N., García-Sansegundo, J., Gallastegui, G., Farias, P., Giacosa, R., Hongn, F. D., et al. (2018). The pre-andean phases of construction of the southern Andes basement in neoproterozoic–paleozoic times. In A. Folguera, E. Contreras-Reyes, N. Heredia, A. Encinas, S. B. Iannelli, V. Oliveros, et al. (Eds.), *The Evolution of the Chilean-Argentinean Andes*. Springer Earth system sciences. (pp. 111–131). Springer International Publishing. https://doi.org/10.1007/978-3-319-67774-3_5
- Hongn, F. D., Del Papa, C. E., Powell, J., Petrinovic, I., Mon, R., & Deraco, V. (2007). Middle Eocene deformation and sedimentation in the Puna-Eastern Cordillera transition (23°–26°S): Control by preexisting heterogeneities on the pattern of initial Andean shortening. *Geology*, *35*(3), 271. <https://doi.org/10.1130/G23189A.1>
- Hongn, F. D., Mon, R., Petrinovic, I., Del Papa, C. E., & Powell, J. (2010). Inversión y reactivación tectónicas cretácico-cenozoicas en el noroeste argentino: Influencia de las heterogeneidades del basamento neoproterozoico-paleozoico inferior. *Revista de la Asociación Geológica Argentina*, *66*(1), 38–53.
- Horton, B. K. (2005). Revised deformation history of the central Andes: Inferences from Cenozoic foredeep and intermontane basins of the Eastern Cordillera, Bolivia. *Tectonics*, *24*(3). <https://doi.org/10.1029/2003TC001619>
- Horton, B. K. (2018). Tectonic regimes of the central and southern Andes: Responses to variations in plate coupling during subduction. *Tectonics*, *37*(2), 402–429. <https://doi.org/10.1002/2017TC004624>
- Hurfurd, A. J., & Green, P. F. (1983). The zeta age calibration of fission-track dating. *Chemical Geology*, *41*, 285–317. [https://doi.org/10.1016/s0009-2541\(83\)80026-6](https://doi.org/10.1016/s0009-2541(83)80026-6)
- Jiron, R. (2015). *Interactions of tectonics, climate, and deposition in intermontane basins on the margin of the Puna Plateau, NW Argentina (PhD thesis)*. University of California.
- Jordan, T. E., Isacks, B. L., Allmendinger, R. W., Brewer, J. A., Ramos, V. A., & Ando, C. J. (1983). Andean tectonics related to geometry of subducted Nazca plate. *The Geological Society of America Bulletin*, *94*(3), 341. [https://doi.org/10.1130/0016-7606\(1983\)94<341:ATRTGO>2.0.CO;2](https://doi.org/10.1130/0016-7606(1983)94<341:ATRTGO>2.0.CO;2)
- Ketcham, R. A., Carter, A., Donelick, R. A., Barbarand, J., & Hurfurd, A. J. (2007). Improved modeling of fission-track annealing in apatite. *American Mineralogist*, *92*(5–6), 799–810. <https://doi.org/10.2138/am.2007.2281>
- Ketcham, R. A., Donelick, R. A., & Carlson, W. D. (1999). Variability of apatite fission-track annealing kinetics: III, Extrapolation to geological time scales. *American Mineralogist*, *84*(9), 1235–1255. <https://doi.org/10.2138/am-1999-0903>
- Ketcham, R. A., Gautheron, C., & Tassan-Got, L. (2011). Accounting for long alpha-particle stopping distances in (U–Th–Sm)/He geochronology: Refinement of the baseline case. *Geochimica et Cosmochimica Acta*, *75*(24), 7779–7791. <https://doi.org/10.1016/j.gca.2011.10.011>
- Kley, J. (1996). Transition from basement-involved to thin-skinned thrusting in the Cordillera Oriental of southern Bolivia. *Tectonics*, *15*(4), 763–775. <https://doi.org/10.1029/95TC03868>

- Kley, J., & Monaldi, C. R. (2002). Tectonic inversion in the Santa Barbara System of the central Andean foreland thrust belt, northwestern Argentina. *Tectonics*, 21(6), 11–11–18. <https://doi.org/10.1029/2002TC902003>
- Kley, J., Monaldi, C. R., & Salfity, J. A. (1999). Along-strike segmentation of the andean foreland: Causes and consequences. *Tectonophysics*, 301(1–2), 75–94. [https://doi.org/10.1016/S0040-1951\(98\)90223-2](https://doi.org/10.1016/S0040-1951(98)90223-2)
- Kley, J., Rossello, E. A., Monaldi, C. R., & Habighorst, B. (2005). Seismic and field evidence for selective inversion of Cretaceous normal faults, Salta rift, northwest Argentina. *Tectonophysics*, 399(1–4), 155–172. <https://doi.org/10.1016/j.tecto.2004.12.020>
- Kortyna, C., DeCelles, P. G., & Carrapa, B. (2019). Structural and thermochronologic constraints on kinematics and timing of inversion of the Salta rift in the Tonco-Amblayo sector of the Andean retroarc fold-thrust belt, northwestern Argentina. In *Andean tectonics* (pp. 429–464). Elsevier. <https://doi.org/10.1016/B978-0-12-816009-1.00018-6>
- Linkimer, L., Beck, S. L., Zandt, G., Alvarado, P., Anderson, M., Gilbert, H., & Zhang, H. (2020). Lithospheric structure of the Pampean flat slab region from double-difference tomography. *Journal of South American Earth Sciences*, 97, 102417. <https://doi.org/10.1016/j.jsames.2019.102417>
- Marquillas, R. A., Del Papa, C. E., & Sabino, I. F. (2005). Sedimentary aspects and paleoenvironmental evolution of a rift basin: Salta Group (Cretaceous–Paleogene), northwestern Argentina. *International Journal of Earth Sciences*, 94(1), 94–113. <https://doi.org/10.1007/s00531-004-0443-2>
- McFarland, P. K., Bennett, R. A., Alvarado, P., & DeCelles, P. G. (2017). Rapid geodetic shortening across the eastern Cordillera of NW Argentina observed by the puna-andes GPS array. *Journal of Geophysical Research: Solid Earth*, 122(10), 8600–8623. <https://doi.org/10.1002/2017JB014739>
- McGroder, M. F., Lease, R. O., & Pearson, D. M. (2015). Along-strike variation in structural styles and hydrocarbon occurrences, Subandean fold-and-thrust belt and inner foreland, Colombia to Argentina. In P. G. DeCelles, M. N. Ducea, B. Carrapa, & P. A. Kapp (Eds.), *Geodynamics of a cordilleran orogenic system: The central Andes of Argentina and northern Chile*. Geological Society of America. [https://doi.org/10.1130/2015.1212\(05\)](https://doi.org/10.1130/2015.1212(05))
- McNaught, M. A., & Mitra, G. (1993). A kinematic model for the origin of footwall synclines. *Journal of Structural Geology*, 15(6), 805–808. [https://doi.org/10.1016/0191-8141\(93\)90064-H](https://doi.org/10.1016/0191-8141(93)90064-H)
- McQuarrie, N. (2002). The kinematic history of the central Andean fold-thrust belt, Bolivia: Implications for building a high plateau. *The Geological Society of America Bulletin*, 114(8), 950–963. [https://doi.org/10.1130/0016-7606\(2002\)114<0950:TKHOTC>2.0.CO;2](https://doi.org/10.1130/0016-7606(2002)114<0950:TKHOTC>2.0.CO;2)
- McQuarrie, N., Barnes, J. B., & Ehlers, T. A. (2008). Geometric, kinematic, and erosional history of the central Andean Plateau, Bolivia (15–17°S). *Tectonics*, 27(3). <https://doi.org/10.1029/2006tc002054>
- Meesters, A. G. C. A., & Dunai, T. J. (2005). A noniterative solution of the (U-Th)/He age equation. *Geochemistry, Geophysics, Geosystems*, 6(4). <https://doi.org/10.1029/2004gc000834>
- Mon, R., Rahmer, S., & Mena, R. (1993). Estructuras superpuestas en la Cordillera Oriental. XII Congreso Geológico Argentino y II Congreso de Exploración de Hidrocarburos, *Actas*, 2, 48–54.
- Montero-López, C., Del Papa, C. E., Hongn, F. D., Strecker, M. R., & Aramayo, A. (2018). Synsedimentary broken-foreland tectonics during the Paleogene in the Andes of NW Argentina: New evidence from regional to centimetre-scale deformation features. *Basin Research*, 30, 142–159. <https://doi.org/10.1111/bre.12212>
- Montero-López, C., Hongn, F. D., López Steinmetz, R. L., Aramayo, A., Pingel, H., Strecker, M. R., et al. (2020). Development of an incipient Paleogene topography between the present-day eastern andean plateau (Puna) and the eastern Cordillera, southern central Andes, NW Argentina. *Basin Research*, 33(2), 1194–1217. <https://doi.org/10.1111/bre.12510>
- Moreno, J. A. (1970). Estratigrafía y paleogeografía del Cretácico superior en la cuenca del noroeste argentino, con especial mención de los Subgrupos Balbuena y Santa Bárbara. *Revista de la Asociación Geológica Argentina*, 24, 9–44.
- Moya, M. C. (1998). El Paleozoico Inferior en la Sierra de Mojotoro, Salta-Jujuy. *Revista de la Asociación Geológica Argentina*, 53(2), 219–238.
- Moya, M. C. (2015). La “Fase Oclógica Ordovícico Superior” en el noroeste argentino: Interpretación histórica y evidencias en contrario. *Contribuciones a la Geología Argentina: Serie Correlación Geológica*, 31(1), 73–110.
- Müller, J. P., Kley, J., & Jacobshagen, V. (2002). Structure and cenozoic kinematics of the eastern Cordillera, southern Bolivia (21°S). *Tectonics*, 21(5), 1–1–1–24. <https://doi.org/10.1029/2001TC001340>
- Otamendi, J. E., Cristofolini, E. A., Morosini, A., Armas, P., Tibaldi, A. M., & Camilletti, G. C. (2020). The geodynamic history of the famatinian arc, Argentina: A record of exposed geology over the type section (latitudes 27°–33° south). *Journal of South American Earth Sciences*, 100, 102558. <https://doi.org/10.1016/j.jsames.2020.102558>
- Parker, S. D., & Pearson, D. M. (2021). Pre-thrusting stratigraphic control on the transition from a thin-skinned to thick-skinned structural style: An example from the double-decker Idaho-Montana fold-thrust belt. *Tectonics*, 40(5). e2020TC006429. <https://doi.org/10.1029/2020TC006429>
- Pascual, R., Bond, M., & Vucetich, M. (1981). El Subgrupo Santa Bárbara (Grupo Salta) y sus vertebrados, cronología, paleoambientes y paleobiogeografía. 8° Congreso Geológico Argentino, *Actas*, (Vol. 3, pp. 743–758).
- Payrola, P., Del Papa, C. E., Aramayo, A., Pingel, H., Hongn, F. D., Sobel, E. R., et al. (2020). Episodic out-of-sequence deformation promoted by Cenozoic fault reactivation in NW Argentina. *Tectonophysics*, 776, 228276. <https://doi.org/10.1016/j.tecto.2019.228276>
- Pearson, D. M., Kapp, P. A., DeCelles, P. G., Reiners, P. W., Gehrels, G. E., Ducea, M. N., & Pullen, A. (2013). Influence of pre-Andean crustal structure on Cenozoic thrust belt kinematics and shortening magnitude: Northwestern Argentina. *Geosphere*, 9(6), 1766–1782. <https://doi.org/10.1130/GES00923.1>
- Pearson, D. M., Kapp, P. A., Reiners, P. W., Gehrels, G. E., Ducea, M. N., Pullen, A., et al. (2012). Major Miocene exhumation by fault-propagation folding within a metamorphosed, early Paleozoic thrust belt: Northwestern Argentina. *Tectonics*, 31(4). <https://doi.org/10.1029/2011tc003043>
- Petroleum Experts (Petex) (2020). MOVE (v2019.1) [software].
- Pfiffner, O. A. (2017). Thick-skinned and thin-skinned tectonics: A global perspective. *Geosciences*, 7(3), 71. <https://doi.org/10.3390/geosciences7030071>
- Pingel, H., Alonso, R. N., Mulch, A., Rohrmann, A., Sudo, M., & Strecker, M. R. (2014). Pliocene orographic barrier uplift in the southern Central Andes. *Geology*, 42(8), 691–694. <https://doi.org/10.1130/G35538.1>
- Pingel, H., Schildgen, T. F., Strecker, M. R., & Wittmann, H. (2019). Pliocene–Pleistocene orographic control on denudation in northwest Argentina. *Geology*, 47(4), 359–362. <https://doi.org/10.1130/G45800.1>
- Pingel, H., Strecker, M. R., Alonso, R. N., & Schmitt, A. K. (2013). Neotectonic basin and landscape evolution in the eastern Cordillera of NW Argentina, Humahuaca basin (~24°S). *Basin Research*, 25(5), 554–573. <https://doi.org/10.1111/bre.12016>
- Rahl, J. M., Harbor, D. J., Galli, C. I., & O’Sullivan, P. (2018). Foreland Basin record of uplift and exhumation of the eastern Cordillera, northwest Argentina. *Tectonics*, 37(11), 4173–4193. <https://doi.org/10.1029/2017TC004955>
- Rak, A. J., McQuarrie, N., & Ehlers, T. A. (2017). Kinematics, exhumation, and sedimentation of the north central Andes (Bolivia): An integrated thermochronometer and thermokinematic modeling approach. *Tectonics*, 36(11), 2524–2554. <https://doi.org/10.1002/2016TC004440>

- Ramos, V. A. (2008). The basement of the central Andes: The arequipa and related terranes. *Annual Review of Earth and Planetary Sciences*, 36(1), 289–324. <https://doi.org/10.1146/annurev.earth.36.031207.124304>
- Ramos, V. A., Cristallini, E. O., & Pérez, D. J. (2002). The pampean flat-slab of the central Andes. *Journal of South American Earth Sciences*, 15(1), 59–78. [https://doi.org/10.1016/S0895-9811\(02\)00006-8](https://doi.org/10.1016/S0895-9811(02)00006-8)
- Reiners, P. W., Spell, T. L., Nicolescu, S., & Zanetti, K. A. (2004). Zircon (U-Th)/He thermochronometry: He diffusion and comparisons with $^{40}\text{Ar}/^{39}\text{Ar}$ dating. *Geochimica et Cosmochimica Acta*, 68(8), 1857–1887. <https://doi.org/10.1016/j.gca.2003.10.021>
- Reiners, P. W., Thomson, S. N., Vernon, A., Willett, S. D., Zattin, M., Einhorn, J. C., et al. (2015). Low-temperature thermochronologic trends across the central Andes, 21°S–28°S. In P. G. DeCelles, M. N. Ducea, B. Carrapa, & P. A. Kapp (Eds.), *Geodynamics of a cordilleran orogenic system: The central Andes of Argentina and northern Chile*. Geological Society of America. <https://doi.org/10.1130/2015.121212>
- Reyes, F., & Salfity, J. A. (1973). Consideraciones sobre la estratigrafía del Cretácico (Subgrupo Pirgua) del noroeste argentino. In *Actas 5th Congreso Geológico Argentino* (pp. 355–385).
- Reynolds, J. H., Galli, C. I., Hernández, R. M., Idleman, B. D., Kotila, J. M., Hilliard, R. V., & Naeser, C. W. (2000). Middle Miocene tectonic development of the transition zone, Salta province, northwest Argentina: Magnetic stratigraphy from the Metán subgroup, sierra de González. *The Geological Society of America Bulletin*, 112(11), 1736–1751. [https://doi.org/10.1130/0016-7606\(2000\)112<1736:MMDOT>2.0.CO;2](https://doi.org/10.1130/0016-7606(2000)112<1736:MMDOT>2.0.CO;2)
- Reynolds, J. H., Hernández, R. M., Galli, C. I., & Idleman, B. D. (2001). Magnetostratigraphy of the quebrada La porcelana section, sierra de Ramos, Salta province, Argentina: Age limits for the Neogene Orán Group and uplift of the southern Sierras Subandinas. *Journal of South American Earth Sciences*, 14(7), 681–692. [https://doi.org/10.1016/S0895-9811\(01\)00069-4](https://doi.org/10.1016/S0895-9811(01)00069-4)
- Rodríguez-Fernández, L. R., Heredia, N., Seggiaro, R. E., & González, M. A. (1999). Estructura andina de la Cordillera Oriental en el área de la Quebrada de Humahuaca, Provincia de Jujuy, NO de Argentina. *Trabajos de Geología*, 21(21), 321–333.
- Roeder, D. (1988). Andean-age structure of Eastern Cordillera (Province of La Paz, Bolivia). *Tectonics*, 7(1), 23–39. <https://doi.org/10.1029/TC007i001p00023>
- Salfity, J. A., & Marquillas, R. A. (1994). Tectonic and sedimentary evolution of the Cretaceous-Eocene Salta Group basin, Argentina. In J. A. Salfity (Ed.), *Cretaceous tectonics of the Andes* (pp. 266–315). Vieweg+Teubner Verlag. https://doi.org/10.1007/978-3-322-85472-8_6
- Sánchez, M., & Salfity, J. A. (1999). La cuenca Cámbrica del Grupo Mesón en el Noroeste Argentino: Desarrollo estratigráfico y paleogeográfico. *Acta Geologica Hispanica*, 34(2–3), 123–139.
- Schildgen, T. F., Robinson, R. A. J., Savi, S., Phillips, W. M., Spencer, J. Q. G., Bookhagen, B., et al. (2016). Landscape response to late Pleistocene climate change in NW Argentina: Sediment flux modulated by basin geometry and connectivity. *Journal of Geophysical Research: Earth Surface*, 121(2), 392–414. <https://doi.org/10.1002/2015JF003607>
- Seggiaro, R. E., Aris, J., Heredia, N., Gallardo, E., Rodríguez, R., Gallastegui, G., & Alonso, J. L. (2008). Estructuras extensionales ordovícicas en la Cordillera Oriental Noroeste Argentino. *XVII Congreso Geológico Argentino, Acta*, (Vol. 1, pp. 43–44).
- Seggiaro, R. E., & Gallardo, E. (2002). Evidencias de tectónica extensional durante el Paleozoico inferior en las quebradas de Coquena y Humahuaca, Cordillera Oriental, Norte Argentino. *XV Congreso Geológico Boliviano* (pp. 279–282).
- Seggiaro, R. E., Gallardo, E., & González, D. (2014). Tectónica superpuesta en la Sierra de Mojotoro, Cordillera Oriental Provincia de Salta. *XIX Congreso Geológico Argentino* (Vol. S22–63, pp. 1669–1670).
- Seggiaro, R. E., Villagrán, C., Celedón, M., Barrabino, E., & Apaza, F. (2017). Reactivación de fallas paleozoicas durante la tectónica andina en la Cordillera Oriental-noroeste argentino. In C. Muruaga & P. Grosse (Eds.), *Ciencias de la Tierra y Recursos Naturales del NOA. Relatorio del XX Congreso Geológico Argentino* (pp. 603–623).
- Siks, B. C., & Horton, B. K. (2011). Growth and fragmentation of the Andean foreland basin during eastward advance of fold-thrust deformation, Puna plateau and Eastern Cordillera, northern Argentina. *Tectonics*, 30(6). <https://doi.org/10.1029/2011TC002944>
- Sobel, E. R., & Seward, D. (2010). Influence of etching conditions on apatite fission-track etch pit diameter. *Chemical Geology*, 271(1–2), 59–69. <https://doi.org/10.1016/j.chemgeo.2009.12.012>
- Sobel, E. R., & Strecker, M. R. (2003). Uplift, exhumation and precipitation: Tectonic and climatic control of late cenozoic landscape evolution in the northern Sierras Pampeanas, Argentina. *Basin Research*, 15(4), 431–451. <https://doi.org/10.1046/j.1365-2117.2003.00214.x>
- Starck, D. (1995). Silurian-Jurassic stratigraphy and basin evolution of Northwestern Argentina. In A. J. Tankard, R. Suárez, & H. J. Welsink (Eds.), *Petroleum basins of South America, American Association of Petroleum Geologists Memoir*. (Vol. 62, pp. 251–267). American Association of Petroleum Geologists.
- Starck, D. (2011). Cuenca Cretácica-Paleógena del Noroeste Argentino. In E. Kozłowski, L. Legarreta, A. Boll, & P. Marshall (Eds.), *Simposio Cuencas Argentinas: Visión actual* (pp. 1–48).
- Starck, D., Gallardo, E., & Schultz, A. (1992). La discordancia precarbónica en la porción argentina de la cuenca de Tarija. *Boletín de Informaciones Petroleras*, 30, 2–14.
- Strecker, M. R., Alonso, R. N., Bookhagen, B., Carrapa, B., Hillel, G. E., Sobel, E. R., & Trauth, M. H. (2007). Tectonics and climate of the southern central Andes. *Annual Review of Earth and Planetary Sciences*, 35(1), 747–787. <https://doi.org/10.1146/annurev.earth.35.031306.140158>
- Streit, R. L., Burbank, D. W., Strecker, M. R., Alonso, R. N., Cottle, J. M., & Kylander-Clark, A. R. (2017). Controls on intermontane basin filling, isolation and incision on the margin of the Puna Plateau, NW Argentina (~23°S). *Basin Research*, 29(S1), 131–155. <https://doi.org/10.1111/bre.12141>
- Suppe, J. (1983). Geometry and kinematics of fault-bend folding. *American Journal of Science*, 283(7), 684–721. <https://doi.org/10.2475/ajs.283.7.684>
- Turner, J. C. M. (1959). Estratigrafía del cordón de Escaya y de la sierra de Rinconada (Jujuy). *Revista de la Asociación Geológica Argentina*, 13, 15–39.
- Turner, J. C. M., & Méndez, V. (1975). Geología del sector Oriental de los departamentos de Santa Victoria e Iruya. Provincia de Salta. República Argentina. *Boletín Nacional de Ciencias*, 51(1–2), 11–24.
- Uba, C. E., Kley, J., Strecker, M. R., & Schmitt, A. K. (2009). Unsteady evolution of the Bolivian Subandean thrust belt: The role of enhanced erosion and clastic wedge progradation. *Earth and Planetary Science Letters*, 281(3–4), 134–146. <https://doi.org/10.1016/j.epsl.2009.02.010>
- Uba, C. E., Strecker, M. R., & Schmitt, A. K. (2007). Increased sediment accumulation rates and climatic forcing in the central Andes during the late Miocene. *Geology*, 35(11), 979. <https://doi.org/10.1130/G224025A.1>
- Vaucher, R., Vaccari, N. E., Balseiro, D., Muñoz, D. F., Dillingier, A., Waisfeld, B. G., & Buatois, L. A. (2020). Tectonic controls on late Cambrian-early ordovician deposition in Cordillera oriental (northwest Argentina). *International Journal of Earth Sciences*, 109(6), 1897–1920. <https://doi.org/10.1007/s00531-020-01879-9>
- Vermeesch, P. (2009). RadialPlotter: A java application for fission track, luminescence and other radial plots. *Radiation Measurements*, 44(4), 409–410. <https://doi.org/10.1016/j.radmeas.2009.05.003>
- Vermeesch, P. (2018). IsoplotR: A free and open toolbox for geochronology. *Geoscience Frontiers*, 9(5), 1479–1493. <https://doi.org/10.1016/j.gsf.2018.04.001>

- Villagrán, C., Seggiaro, R. E., Gallardo, E., Pereyra, R., Barrabino, E., & Celedón, M. (2015). Análisis estructural en los alrededores del Cerro Gólgota, Quebrada del Toro, Salta. In C. Muruaga & P. Grosse (Eds.), *Ciencias de la Tierra y Recursos Naturales del NOA. Relatorio del XX Congreso Geológico Argentino, San Miguel de Tucumán* (pp. 110–111). Tucumán.
- Viramonte, J. G., Kay, S., Becchio, R., Escayola, M. P., & Novitski, I. (1999). Cretaceous rift related magmatism in central-western South America. *Journal of South American Earth Sciences*, *12*(2), 109–121. [https://doi.org/10.1016/S0895-9811\(99\)00009-7](https://doi.org/10.1016/S0895-9811(99)00009-7)
- Wagner, G. A., Gleadow, A., & Fitzgerald, P. G. (1989). The significance of the partial annealing zone in apatite fission-track analysis: Projected track length measurements and uplift chronology of the transantarctic mountains. *Chemical Geology: Isotope Geoscience section*, *79*(4), 295–305. [https://doi.org/10.1016/0168-9622\(89\)90035-3](https://doi.org/10.1016/0168-9622(89)90035-3)
- Wolf, R. A., Farley, K. A., & Kass, D. (1998). Modeling of the temperature sensitivity of the apatite (U–Th)/He thermochronometer. *Chemical Geology*, *148*(1–2), 105–114. [https://doi.org/10.1016/S0009-2541\(98\)00024-2](https://doi.org/10.1016/S0009-2541(98)00024-2)
- Yates, D., Moore, D. S., & McCabe, G. P. (1999). *The practice of statistics*. Freeman.
- Zapata, S., Sobel, E. R., Del Papa, C. E., Muruaga, C., & Zhou, R. (2019). Miocene fragmentation of the Central Andean foreland basins between 26 and 28°S. *Journal of South American Earth Sciences*, *94*, 102238. <https://doi.org/10.1016/j.jsames.2019.102238>
- Zhou, R., Schoenbohm, L. M., Sobel, E. R., Davis, D. W., & Glodny, J. (2017). New constraints on orogenic models of the southern Central Andean Plateau: Cenozoic basin evolution and bedrock exhumation. *The Geological Society of America Bulletin*, *129*(1–2), 152–170. <https://doi.org/10.1130/B31384.1>